

Università degli studi di Padova  
Dipartimento di Fisica e Astronomia

Tesi di Dottorato

# Search for heavy resonances decaying into a $Z$ boson and a vector boson in the $\nu\bar{\nu} q\bar{q}$ final state at CMS

Supervisor: Prof. Franco Simonetto  
Candidate: Lisa Benato

Scuola di Dottorato di Ricerca, XXX ciclo



"I have no special talent. I am only passionately curious."

(A. Einstein)



# Contents

<b>1</b>	<b>Introduction</b>	<b>1</b>
<b>2</b>	<b>Theoretical motivation</b>	<b>3</b>
<b>3</b>	<b>The Large Hadron Collider and the CMS experiment</b>	<b>5</b>
3.1	The Large Hadron Collider . . . . .	5
3.1.1	Proton-proton interactions . . . . .	8
3.2	CMS detector . . . . .	9
3.2.1	The coordinate system . . . . .	10
3.2.2	The magnet . . . . .	11
3.2.3	The tracking system . . . . .	12
3.2.3.1	The pixel detector . . . . .	12
3.2.3.2	The strip detector . . . . .	13
3.2.4	The electromagnetic calorimeter . . . . .	13
3.2.5	The hadronic calorimeter . . . . .	14
3.2.6	The muon system . . . . .	15
3.2.6.1	The Drift Tubes . . . . .	15
3.2.6.2	The Cathode Strip Chambers . . . . .	16
3.2.6.3	The Resistive Plate Chambers . . . . .	16
3.2.7	The trigger system and data acquisition . . . . .	16
3.2.7.1	The Level-1 trigger . . . . .	17
3.2.7.2	The High Level Trigger . . . . .	17
3.2.7.3	Data acquisition, computing and storage . . . . .	17
3.2.8	Particle Flow event reconstruction . . . . .	18
3.2.9	Physics objects . . . . .	18
3.2.9.1	Track reconstruction . . . . .	18
3.2.9.2	Vertices reconstruction . . . . .	19
3.2.9.3	Electrons and photons reconstruction . . . . .	19
3.2.9.4	Muon reconstruction . . . . .	20
3.2.9.5	Jet reconstruction . . . . .	20
3.2.9.6	Tau reconstruction . . . . .	22
3.2.9.7	b-jets tagging . . . . .	22
3.2.9.8	Missing transverse energy reconstruction . . . . .	25

3.3 ATLAS, ALICE, LHCb detectors .....	28
3.3.1 ATLAS .....	28
3.3.2 ALICE .....	29
3.3.3 LHCb .....	29

1

## **Abstract**

2

3

**CONTENTS**

---

---

# Introduction



# Theoretical motivation



# The Large Hadron Collider and the CMS experiment

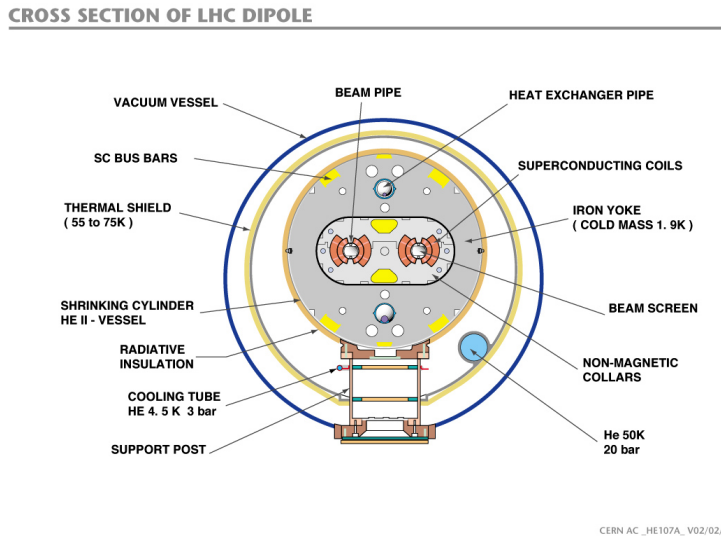
## 3.1 The Large Hadron Collider

14 The Large Hadron Collider (LHC) [1] is a 27 km ring structure designed for the acceleration and  
 15 collision of protons and heavy ions. It is situated approximatively 100 m underground, between  
 16 France and Switzerland, in the Geneva area, and it is part of the CERN research facilities. In order to  
 17 reduce the cost of the project, approved in 1996, the LHC has been designed to fit the pre-existing  
 18 underground tunnel of the Large Electron-Positron collider (LEP), built to accelerate electrons and  
 19 positrons and running until the year 2000.

20 Moving from an electron-positron collider to an hadron collider allowed to reach higher energies  
 21 in the center-of-mass frame, since the synchrotron radiation loss is inversely proportional to the  
 22 fourth power of the mass of the particle involved: hence, the radiation is reduced by a factor  $m_p/m_e \sim$   
 23  $10^3$ . The choice of a proton-proton collider was driven also by the possibility to collect higher lumi-  
 24 nosities (and hence more statistics) with regards to, for example, a proton-antiproton collider, like  
 25 Tevatron at Fermilab, in the USA.

26 In the LHC two identical beam pipes are designed to let protons circulate in opposite directions, in  
 27 ultrahigh vacuum conditions ( $10^{-11}$ – $10^{-10}$  mbar), to avoid spurious collisions with gas molecules.  
 28 Given the reduced diameter of the tunnel (4 m), the two proton beams are magnetically coupled.  
 29 The collider is composed by 8 arc sections (48 km) driving protons around the ring, and straight  
 30 sections (6 km) where beam control systems and detectors are inserted. Proton beams collide in  
 31 four interaction points, where the main LHC experiments are installed: ALICE, ATLAS, CMS, LHCb.

32 In fig. 3.1, a slice of the arc section is displayed. Around the beam pipes, two superconducting  
 33 magnetic dipoles are located: they generate vertical magnetic fields in opposite directions. The  
 34 superconducting coils are made of niobium-titanium, materials that are superconducting at very  
 35 low temperature. At the LHC, they are kept at a temperature of 1.9 K (-271.3°C) by a closed liq-  
 36 uid helium circuit. A current of 11850 A flows through the magnets, without any energy loss due  
 37 to electrical resistance, generating a magnetic field of 8.33 T. Magnets of higher order in multipole  
 38 expansion (quadrupoles, sextupoles, octupoles, etc.) are employed to optimize the proton trajec-  
 39 tories; in particular, quadrupoles allow to focus and squeeze the beams. Along the LHC ring there  
 40 are 9593 magnets; 1232 are dipoles, 392 are quadrupoles.



CERN AC \_HE107A\_ V02/02/98

Figure 3.1: Section of the LHC dipole magnet structure.

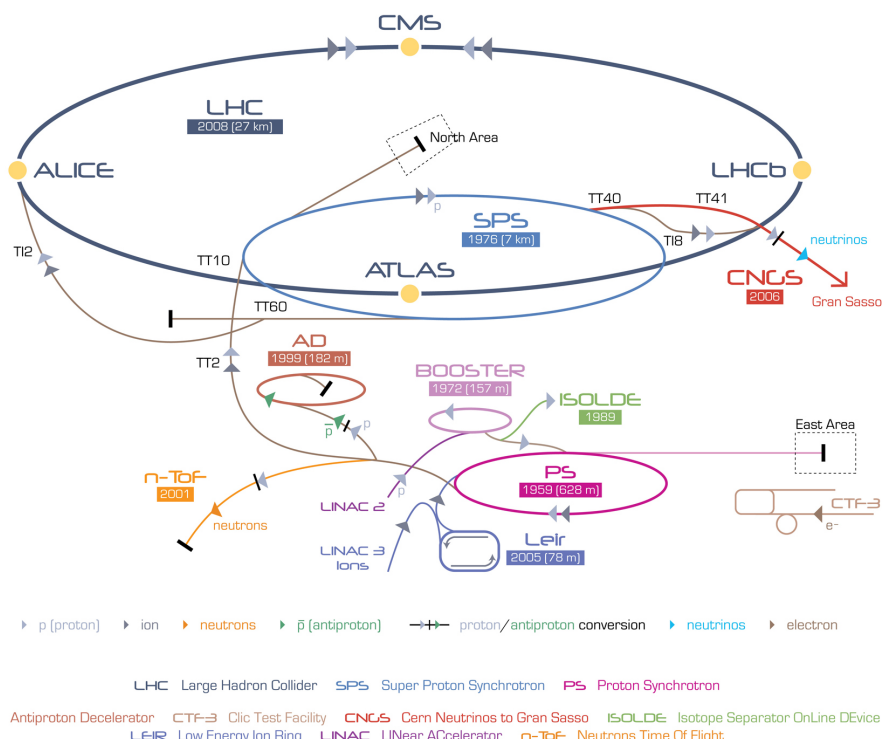


Figure 3.2: The CERN accelerator complex.

- 41 The LHC represents the final step of the CERN accelerator complex, showed in fig. 3.2. Protons are  
 42 extracted from hydrogen atoms and inserted in the linear accelerator Linac2, that brings them to an  
 43 energy of 50 MeV. They circulate around a little synchrotron, Proton Synchrotron Booster, reaching  
 44 an energy of 1.4 GeV, and then in the Proton Synchrotron (PS), where their energy is increased to 25  
 45 GeV. The second to last step is the Super Proton Synchrotron, SPS, accelerating protons up to 450  
 46 GeV. They are finally injected in the Large Hadron Collider, where sixteen radiofrequency cavities  
 47 (RF) accelerate protons inside each beam up to an energy of 6.5 TeV, corresponding to a center-of-

### 3.1 The Large Hadron Collider

---

mass energy of 13 TeV when colliding. The RF cavities provide an accelerating electromagnetic field up to 5 MV/m (maximum voltage of 2 MV), that oscillates with a frequency of 400 MHz. Like the magnets, the cavities are kept at low temperature (4.5 K, or -268.7°C) in order to allow superconducting conditions. The maximum beam energy can be reached in 15 minutes. After several hours of collisions ( $\sim 10$  hours), the quality of the beams deteriorates and they are extracted from the machine and dumped.

Protons circulate inside the LHC ring in bunches of  $\sim 10^{11}$  particles each, 80 mm long. Focusing magnets allow to reduce the bunch diameter down to 16  $\mu\text{m}$ . Different bunches are separated by 25 ns (or,  $\sim 7.5$  m), corresponding to a frequency of 40 MHz and an instantaneous (peak) luminosity (defined in eq. 3.1) of  $1.2 \times 10^{34} \text{ cm}^{-2}\text{s}^{-1}$ . Given the structure of the beams, at every bunch crossing many protons interact simultaneously: this phenomenon is called pile-up. The designed maximum number of bunches per fill is 2808.

61

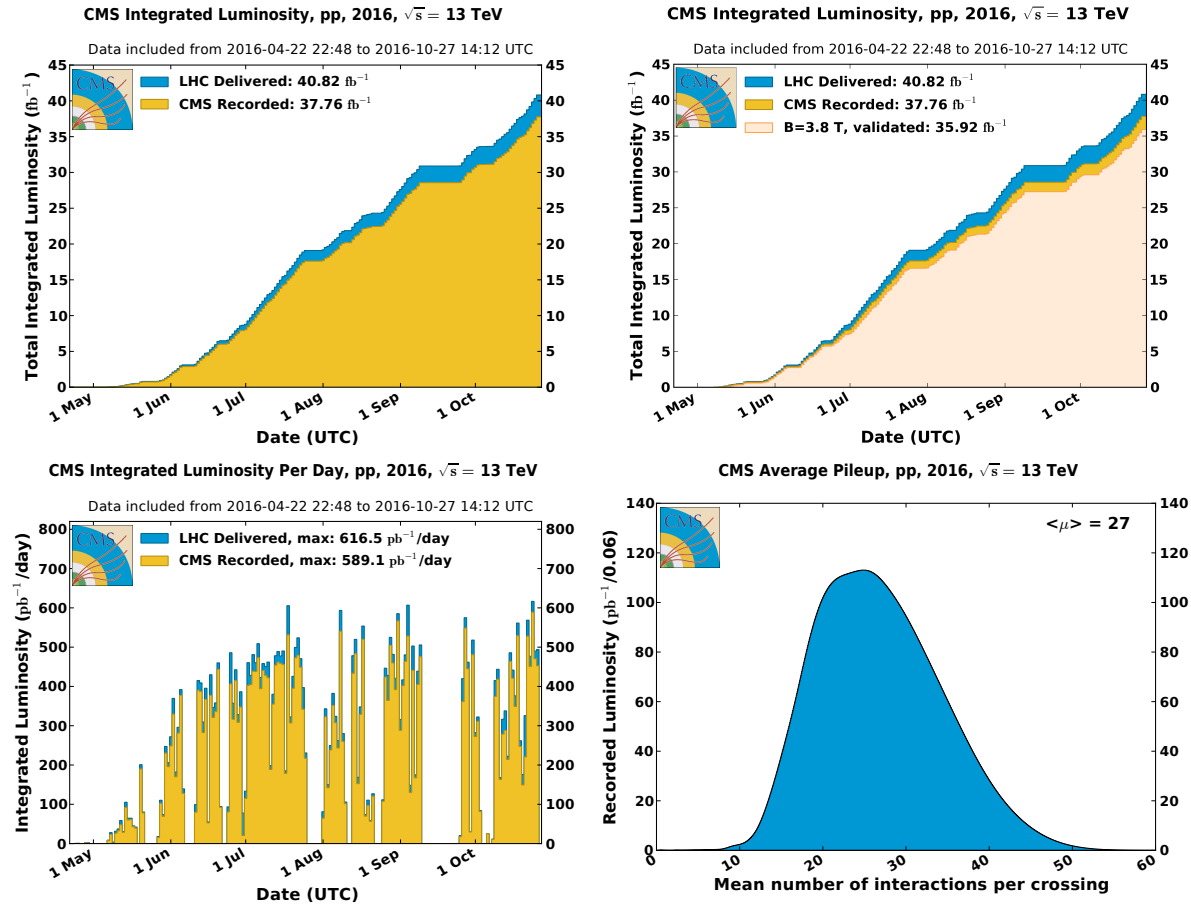


Figure 3.3: Luminosity in 2016 LHC data. Top-left plot: the cumulative integrated luminosity delivered by LHC (in blue) and recorded by CMS (in orange), as a function of the data taken period. Top-right plot: data recorded by CMS and declared as optimal for the physics analyses (in light orange), corresponding to a total integrated luminosity of  $35.9 \text{ fb}^{-1}$ . Bottom-left plot: maximum integrated luminosity per day. Bottom-right plot: number of proton interactions per bunch crossing (pile-up).

62 The main parameters characterizing an hadronic collider are the center-of-mass energy, correspond-  
63 ing to the sum of the energies of the beams, and the instantaneous luminosity, that describes the

64 frequency of the interactions among the bunches in the beams. If the bunches in the first beam  
 65 contain  $n_1$  protons, and the bunches in the second beam contain  $n_2$  protons, and if the colliding  
 66 area is  $\Sigma$ , the frequency of complete turns around the ring is  $f$ , the instantaneous luminosity  $\mathcal{L}_{\text{inst}}$   
 67 is:  
 68

$$\mathcal{L}_{\text{inst}} = f \frac{n_1 n_2}{\Sigma}. \quad (3.1)$$

68 If a generic physics process  $i$  has a cross-section of  $\sigma_i$ , the interaction rate  $R_i$  is:  
 69

$$R_i = \frac{dN_i}{dt} = \sigma_i \mathcal{L}_{\text{inst}}, \quad (3.2)$$

69 and the number of events recorded in the time interval  $(0, \tau)$  is obtained from the integrated lumi-  
 70 nosity  $\mathcal{L} = \int_0^\tau \mathcal{L}_{\text{inst}} dt$ :  
 71

$$N_i = \sigma_i \int_0^\tau \mathcal{L}_{\text{inst}} dt. \quad (3.3)$$

71 In fig. 3.3, a summary of the luminosity measurement in 2016 data is presented. The luminosity  
 72 delivered by LHC is represented in blue, the recorded by CMS is in orange. The mean number of in-  
 73 teraction per bunch crossing (pile-up) is presented as well. The average number of interactions per  
 74 collision is 27, the maximum is around 50 (in fig. 3.4, a record of 78 pile-up collisions was detected).  
 75

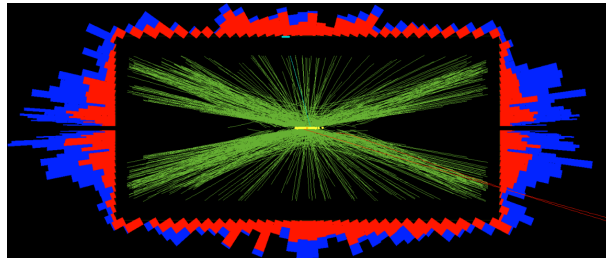


Figure 3.4: CMS collision event, where a record of 78 interactions per single bunch crossing were taking place simultaneously.

### 75 3.1.1 Proton-proton interactions

76 Proton-proton collisions allow to reach high energies and luminosities, but the drawback is the  
 77 complexity of the events when compared to electron-positron collisions: not only because of the  
 78 increasing backgrounds due to strong interactions among partons, but also because the momenta  
 79 of the proton partons taking part in the interaction are unknown; not to mention the problem of dis-  
 80 entangling the tracks of the particles coming from the interesting hard interactions from the spec-  
 81 tator pile-up interactions.  
 82

82 The majority of the LHC events is represented by soft interactions, with low transverse momen-  
 83 tum transfer, namely elastic and diffractive scatterings. In the so-called hard interactions, on the  
 84 other hand, the transferred momentum among particles is high, allowing to produce massive reso-  
 85 nant phenomena. These events manifest in peculiar final state signatures that can be distinguished  
 86 from the soft background interactions.  
 87

87 At high momentum transfer (perturbative regime), a proton can be described as a collection of par-  
 88 tons, each bringing a fraction  $x$  of the initial beam momentum, whose distribution is described by  
 89 the parton distribution functions (PDF),  $f(x, Q^2)$ , as a function of the Bjorken's variable and of the  
 90

### 3.2 CMS detector

---

momentum transfer  $Q^2$ . At very high center-of-mass energies (13 TeV), the proton mass can be neglected; the available energy in the parton 1 – parton 2 scattering is unknown,  $\sqrt{x_1 x_2 s}$ . The total cross-section is given by:

$$\sigma = \int dx_1 f_1(x_1, Q^2) \int dx_2 f_2(x_2, Q^2) \sigma_{12}(x_1 p_1, x_2 p_2, Q^2), \quad (3.4)$$

where  $\sigma_{12}$  is the cross-section at parton level, and  $f_1, f_2$  are the parton PDFs. In fig. 3.5, parton cross-sections of the main standard model processes are displayed, as a function of the center-of-mass energy.

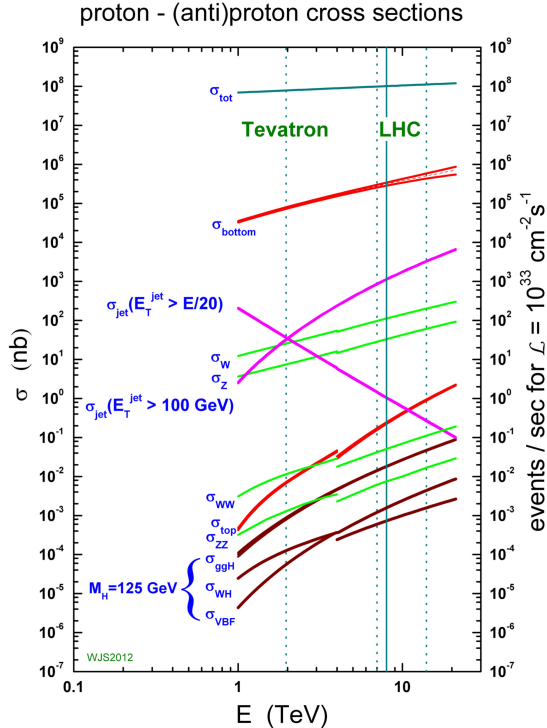


Figure 3.5: Cross-sections and number of expected events in proton-proton collisions, as a function of the center-of-mass energy. Rare phenomena, such as the Higgs boson production, can be observed at the LHC.

### 3.2 CMS detector

The Compact Muon Solenoid (CMS) is a multi-purpose detector built in the LHC ring. It is situated in a cavern 100 m underground, near Cessy, in France. It is a cylinder 22 m long, with a diameter of 15 m, and a weight of 12500 tons. Its physics programme includes the search for the Higgs boson (discovered in 2012), precision measurements of the Standard Model parameters and rare decays (physics of beauty quark), and search for new physics beyond the standard model (SUSY, exotic phenomena, dark matter, extra dimensions).

The CMS detector is structured in many layers of sub-detectors, giving different responses depending on the nature and the momentum of the particles passing through. The inner detectors have been finely segmented in order to afford the high radiation levels and particle multiplicity at the

106 interaction point, so that the reduced occupancy of each layer allows to measure and distinguish  
 107 precisely the primary vertices of the hard interactions from the pile-up events. A very accurate time  
 108 resolution is necessary to synchronize all the subsystems together.

109

## CMS Detector

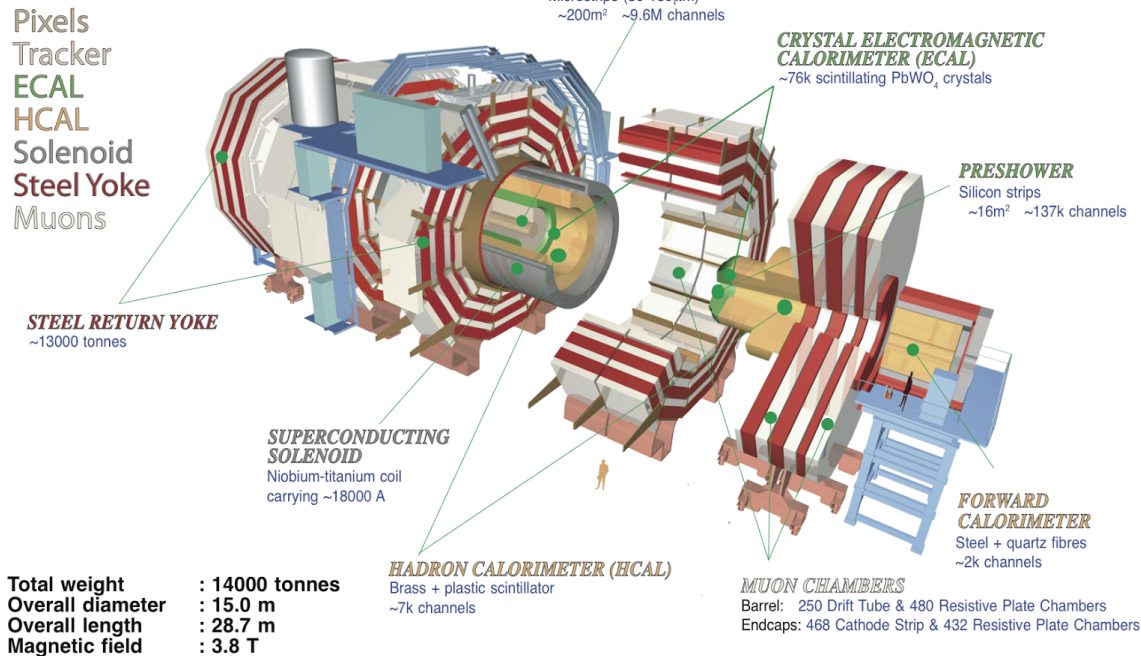


Figure 3.6: The CMS experiment.

110 Fig. 3.6 shows a sketch of the CMS detector. It is longitudinally segmented in the barrel region and  
 111 two endcaps. In the forward region (over the endcaps), where the beam radiation is very intense,  
 112 additional calorimeters have been placed. In fig. 3.7, the mean path of a specific particle through  
 113 the sub-detectors is represented, depending on its flavour.  
 114 A detailed description of the CMS detector can be found in [2].

### 115 3.2.1 The coordinate system

116 The CMS coordinate system is depicted in fig. 3.8.  $x$  and  $y$  are the coordinates in the transverse  
 117 plane,  $z$  is the longitudinal coordinate. The  $x$  axis points at the center of the LHC ring, the  $y$  axis  
 118 points upward, the  $z$  axis is along the beam direction. The azimuthal angle  $\phi$  lies in the transverse  
 119 plane, and it is measured starting from the  $x$  axis; the radial coordinate is  $r$ . The polar angle  $\theta$  lies  
 120 in the plane  $rz$ . The transverse component of the 3-momentum,  $\vec{p}_T$ , is orthogonal to the beam axis  
 121 and lies in the plane  $xy$ . The transverse energy is defined as the magnitude of  $\vec{p}_T$ :  $E_T = E \sin \theta$ .  
 122 Two other commonly used variables are the rapidity,  $\mathcal{Y}$ , and pseudorapidity,  $\eta$ , defined as functions  
 123 of the particle energy  $E$ , the longitudinal component of the momentum  $p_z$  and the 3-momentum

### 3.2 CMS detector

---

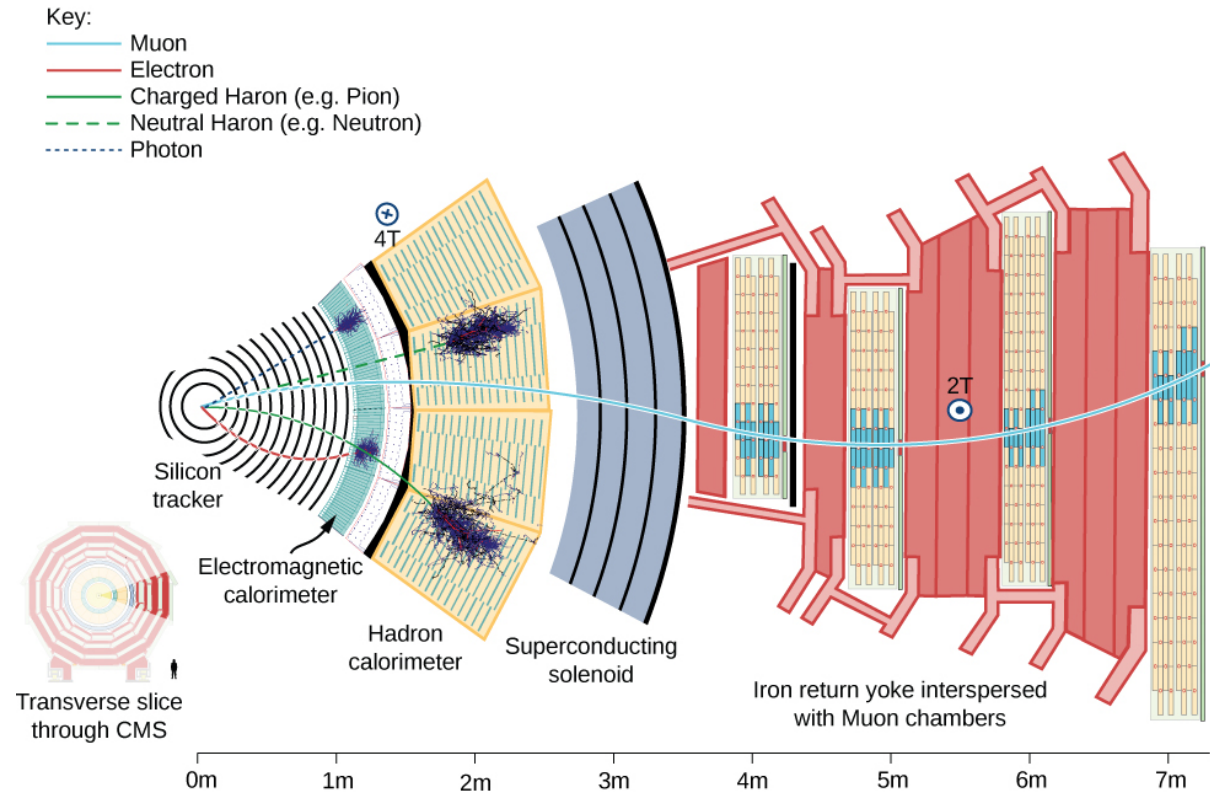


Figure 3.7: Mean path of a particle through the CMS detector. A muon, in light blue, passes through with a bended trajectory, depending on its momentum and charge, triggering signals in all the subsystems. An electron, in red, leaves a track in the silicon tracker and is absorbed by the electromagnetic calorimeter. A neutral or charged hadron, in green, stops inside the hadronic calorimeter. A photon, dotted blue line, showers in the electromagnetic calorimeter, without leaving any track in the silicon detector.

<sup>124</sup> modulus:

$$\begin{aligned} \gamma &= \frac{1}{2} \log \frac{E + p_z}{E - p_z} \\ \eta &= \frac{1}{2} \log \frac{|\vec{p}| + p_z}{|\vec{p}| - p_z} = -\log \tan \frac{\theta}{2} \end{aligned} \quad (3.5)$$

<sup>125</sup> When the considered particle is produced in the forward region, hence at  $\theta = 0$ , it means that  
<sup>126</sup>  $\eta \rightarrow \infty$ . When the particle is produced in the transverse plane, hence  $\theta = \pi/2$ ,  $\eta = 0$ . At high  
<sup>127</sup> energies, when the masses can be neglected, rapidity and pseudorapidity coincide; these variables  
<sup>128</sup> are largely used at colliders because they are invariant under Lorentz boosts along the beam direc-  
<sup>129</sup> tion.

#### 130 3.2.2 The magnet

<sup>131</sup> The CMS superconducting magnet is an hollow cylinder (13 m long, 6 m of diameter, showed in  
<sup>132</sup> fig. 3.9). An electrical current of 19 kA flows through the niobium and titanium fibers that consti-  
<sup>133</sup> tute the solenoid, providing a maximum magnetic field of 3.8 T and storing a maximum energy of  
<sup>134</sup> 2.6 GJ. Superconducting conditions are mantained by a liquid helium cooling system, keeping the  
<sup>135</sup> solenoid temperature at 4.5 K. In order to avoid stray fields, the magnetic field lines are closed by

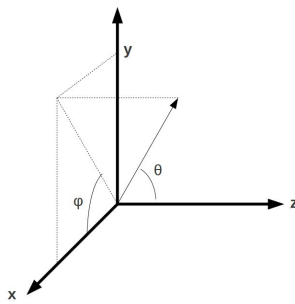


Figure 3.8: CMS coordinate system.

136 the return yoke, composed by 10 ktons of magnetized iron blocks, located in the outer part of CMS  
 137 and alternated to the muon chambers. The homogeneous magnetic field inside the detector bends  
 138 the trajectories of the charged particles, allowing the measurement of their momenta  $p$ , given the  
 139 relation with the magnetic field strength  $B$  and the radial coordinate  $r$  of the trajectory:

$$p[\text{GeV}] = 0.3 \times B[\text{T}] \times r[\text{m}]. \quad (3.6)$$

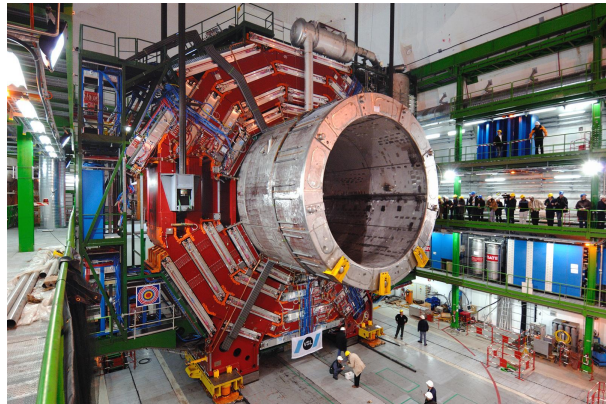


Figure 3.9: Installation of the superconducting solenoid in the CMS cavern.

### 140 3.2.3 The tracking system

141 The CMS tracking system [3,4] is composed by a cylinder of silicon detectors (2.5 m of diameter and  
 142 5.8 m length). Their design guarantees a precise reconstruction of the tracks left by charged particles  
 143 and of the interaction vertices, a fundamental tool to identify heavy quarks (charm, beauty) and  
 144 leptons (taus). Tracker detectors cover a pseudorapidity region of  $|\eta| < 2.5$  and have an active area  
 145 of  $210 \text{ m}^2$ . The two sub-detectors of the tracking system are the pixel detector, installed close to the  
 146 interaction point, and the strip detector, covering a radius of 0.2 – 1.2 m. The high granularity of  
 147 the pixels and strips allows to keep the occupancy at acceptable levels, given the high multiplicity  
 148 of the tracks ( $\sim 1 \text{ MHz/mm}^2$ ). The silicon detectors and the electronic cables are cooled down to a  
 149 temperature of  $\sim 10^\circ \text{ C}$ . The structure of the tracking system is showed in fig. 3.10.

#### 150 3.2.3.1 The pixel detector

151 The pixel detector is composed by 66 millions of silicon cells, whose dimensions are  $100 \times 150 \mu\text{m}^2$ ,  
 152 285  $\mu\text{m}$  of thickness, placed in 1440 modules. Silicon cells are set in three layers in the barrel re-

### 3.2 CMS detector

---

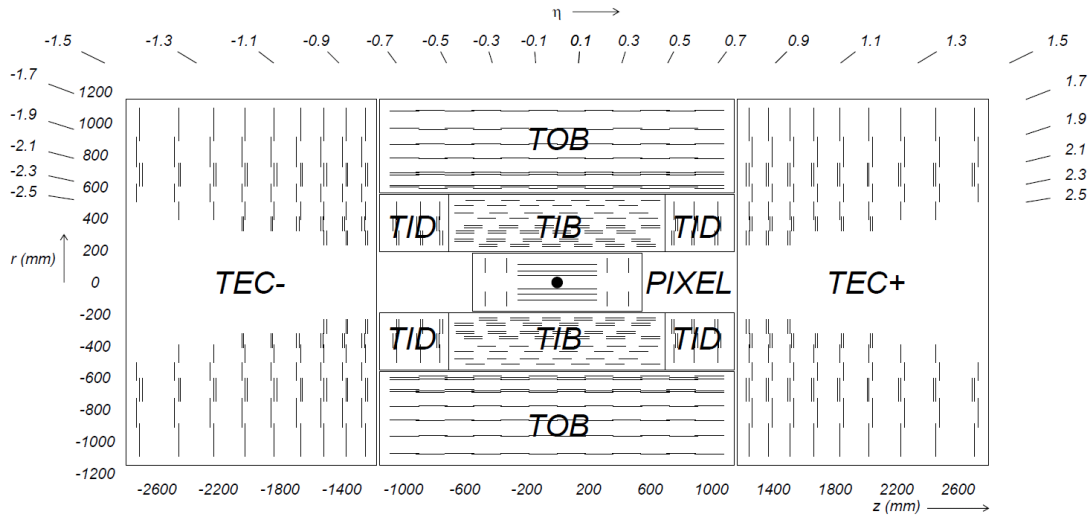


Figure 3.10: The CMS tracking system: the inner pixel detector, close to the interaction point, and the outer strip detector.

153 gion and in two disks at each endcap. Barrel modules are disposed parallel to the magnetic field,  
 154 whilst at the endcap they are tilted by about 20°. Pixels allow a spatial resolution of 10  $\mu\text{m}$  in the  
 155 transverse plane, and of  $\sim 20 \mu\text{m}$  along the longitudinal coordinate. Their reduced size guarantees  
 156 an occupancy of  $10^{-4}$  per pixel at each bunch crossing, in high luminosity regime.

157 **3.2.3.2 The strip detector**

158 The strip system is divided in the four-layered tracker inner barrel (TIB), covering a region  $20 < r <$   
 159 55 cm with respect to the interaction point, the six-layered tracker outer barrel (TOB), located at  
 160  $55 < r < 110$  cm, the three tracker inner disks (TID) and the nine tracker endcaps (TEC) at each  
 161 cylinder base. Given the lower radiation level at higher radii (and hence a lower occupancy, around  
 162 few percent), strips are bigger than the pixels. Silicon strips in TIB and TID are 320  $\mu\text{m}$  thick, 10  
 163 cm long, and with a pitch ranging from 80 to 120  $\mu\text{m}$ ; strips in TOB and TEC are 25 cm long, with a  
 164 different thickness (320  $\mu\text{m}$  for TID, 500  $\mu\text{m}$  for TEC) and pitch (97–184  $\mu\text{m}$ ). There are 15148 strip  
 165 modules, and 9.3 million readout channels. The strip spatial resolution is about 20 – 50  $\mu\text{m}$  in the  
 166 transverse plane and about 200 – 500  $\mu\text{m}$  along the longitudinal coordinate.

167 **3.2.4 The electromagnetic calorimeter**

168 The CMS electromagnetic calorimeter (ECAL, shown in fig. 3.11) [5] is a homogeneous detector com-  
 169 posed by lead tungstate ( $\text{PbWO}_4$ ) scintillating crystals, designed to measure the energy deposits of  
 170 photons and electrons through their electromagnetic showers.  $\text{PbWO}_4$  is transparent and dense (8.3  
 171 gr/cm<sup>3</sup>); it has a fast time response (the 85% of the scintillating light is emitted at every bunch cross-  
 172 ing, namely 24 ns), high scintillating efficiency and radiation resistance; it has a radiation length is  
 173  $X_0 = 0.89$  cm and a Molière radius of 2.19 cm. The ECAL is divided in the barrel region ( $\eta < 1.479$ , at  
 174 a radius of 1.3 m) and the endcaps ( $1.479 < \eta < 3$ ). The 61200 crystals employed in the barrel region,  
 175 whose size is  $(22 \times 22)$  mm<sup>2</sup>  $\times$  23 cm, have a radiation length of  $25.8X_0$ ; the 7324 crystals in the end-  
 176 caps,  $28.6 \times 28.6$  mm<sup>2</sup>  $\times$  22 cm, have a radiation length of  $24.7X_0$ . Before the endcaps, on each side,  
 177 a pre-shower detector is installed: it is composed by two disks of lead absorber and two layers of  
 178 silicon strips, of a radiation length up to  $3X_0$ . The pre-shower calorimeter has been designed to dis-

179 distinguish the photons coming from the  $\pi^0$  decay, from the photons produced in the rare Higgs decay  
 180  $H \rightarrow \gamma\gamma$ . The readout and amplification of the scintillating light, performed by avalanche photodiodes  
 181 in the barrel and by vacuum phototriodes in the endcaps, requires a stable temperature of 18°  
 182 C, mantained by a water cooling system.

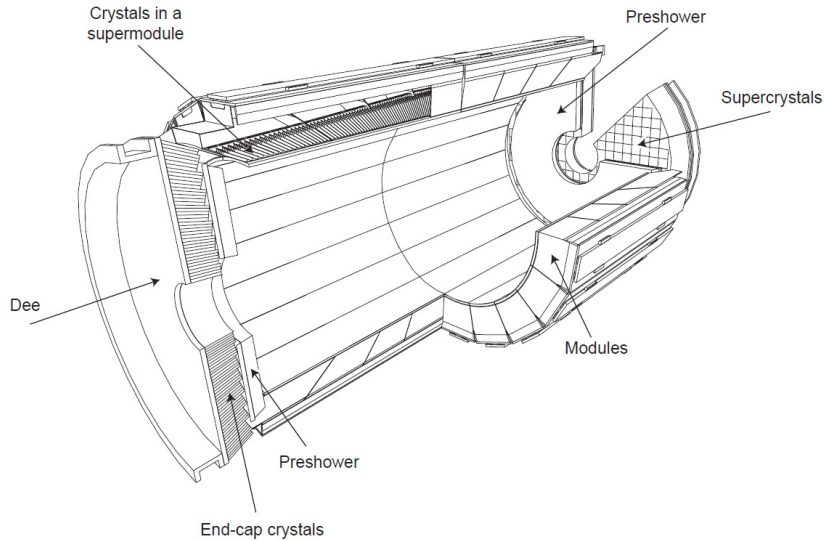


Figure 3.11: The CMS electromagnetic calorimeter.

183 The energy resolution of the calorimeter is parametrized as:

$$\left(\frac{\sigma}{E}\right)^2 = \left(\frac{S}{\sqrt{E}}\right)^2 + \left(\frac{N}{E}\right)^2 + C^2, \quad (3.7)$$

184 where  $S = 0.018 \text{ GeV}^{\frac{1}{2}}$  is the stochastic term,  $N = 0.04 \text{ GeV}$  is related to noise contribution, and  
 185  $C = 0.005$  is a constant term depending on the calibration.

### 186 3.2.5 The hadronic calorimeter

187 The hadronic calorimeter (HCAL, displayed in fig. 3.12) [6] is a sampling calorimeter, composed by  
 188 brass and plastic scintillator layers. It has been designed to guarantee a good hermeticity, allowing  
 189 to perform a precise measurement of the missing transverse energy. It is located within the electro-  
 190 magnetic calorimeter and the solenoid, covering a region of  $|\eta| < 1.3$  in the barrel, and  $1.3 < |\eta| < 3$  in  
 191 the endcaps. Brass is non-magnetic and has short interaction length (16.4 cm): the 60 mm thick ab-  
 192 sorber layers used in the barrel reach 5.6 interaction lengths at  $\eta = 0$  and 10.8 interaction lenghts at  
 193  $\eta = 1.3$ ; the 80 mm thick layers in the endcaps reach 11 interaction lenghts. An additional calorimet-  
 194 ric layer has been installed out of the solenoid, in order to reach 11.8 interaction lenghts in the barrel  
 195 region. The scintillation light, typically in the blue-violet region of the electromagnetic spectrum, is  
 196 collected by wavelength-shifter fibers, translated and amplified by multi-channel hybrid photodi-  
 197 odes, proportionally to the magnitude of the energy deposits. An additional hadronic calorimeter  
 198 (HF) has been placed in the forward region,  $3 < |\eta| < 5.2$ , at 11.2 m from the interaction point. It has  
 199 beeен studied to afford the high levels of radiations: it is composed by 55 mm thick absorber layers  
 200 of stainless-steel, and quartz fibers, able to detect the Cherenkov scintillating light of the charged  
 201 particles of the hadronic showering. A longitudinally segmentation allow to distinguish hadronic

### 3.2 CMS detector

---

202 particles from electromagnetic components. The energy resolution of the hadronic calorimeter is:

$$\left(\frac{\sigma}{E}\right) \approx \frac{a}{\sqrt{E}} \oplus b\%, \quad (3.8)$$

203 where  $a = 65\%$  in the barrel region,  $85\%$  in the endcaps,  $100\%$  in the forward region, and  $b = 5\%$ .

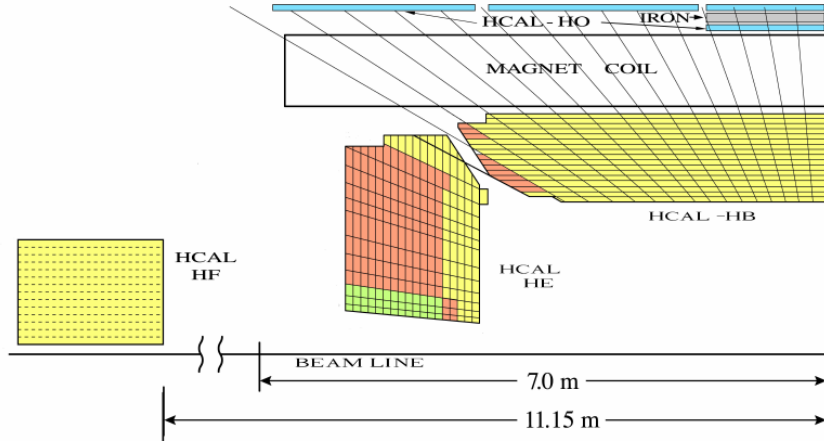


Figure 3.12: The CMS hadronic calorimeter.

#### 204 3.2.6 The muon system

205 The outer system of the CMS experiment consists into gas detectors for identifying muons [7], that  
206 are located between the iron return yokes, designed to close the magnetic field generated by the  
207 solenoid. In the barrel region, where a smaller number of muons is expected and the magnetic field  
208 is less strong, Drift Tubes (DT) detectors are installed. In the endcaps, where the flux of particles is  
209 larger, Cathod Strip Chambers (CSC) are used, and disposed in three disks. CSCs are designed to  
210 allow faster responses, higher granularity and radiation resistance. Resistive Plate Chambers (RPC)  
211 are installed both in the barrel and in the endcaps as additional triggering system. The geometry of  
212 the muon system is showed in fig. 3.13; it consists of 250 DTs, 530 CSCs, 610 RPCs, and it covers a  
213 region  $|\eta| < 2.4$ .

##### 214 3.2.6.1 The Drift Tubes

215 Drift Tube detectors cover a region of  $|\eta| < 1.2$  and are arranged in four stations, segmented along the  
216 beam line in five wheels. The basic element of the detector is the cell, that has a size of  $42 \times 13 \text{ mm}^2$ .  
217 Each cell is filled with a gas mixture (85% argon, 15%  $\text{CO}_2$ ), in which the process of ionization takes  
218 places; the ionization electrons drift from the  $50 \mu\text{m}$  thick steel anodic wire, located in the center  
219 of the cell, towards the aluminium cathodic strips, located at its edge. Additional electrodes on the  
220 surface of the cells allows to shape the electric field, in order to make the drift speed of the electrons  
221 uniform: the muon position is then extrapolated from the measurement of the drift time. Every  
222 station is composed by three cells superlayers. In the inner and the outer superlayers, the cells are  
223 oriented such in a way that the anodic wire is located along the  $z$  axis, to measure the  $\phi$  coordinate.  
224 In the intermediate superlayer, wires are parallel to the radial coordinate, hence they can measure  
225 the  $z$  position. The spatial resolution of the system is  $100 \mu\text{m}$  in the  $(r, \phi)$  plane,  $1 \text{ mrad}$  in the  $\phi$   
226 coordinate, and  $150 \mu\text{m}$  in the longitudinal  $z$  coordinate.

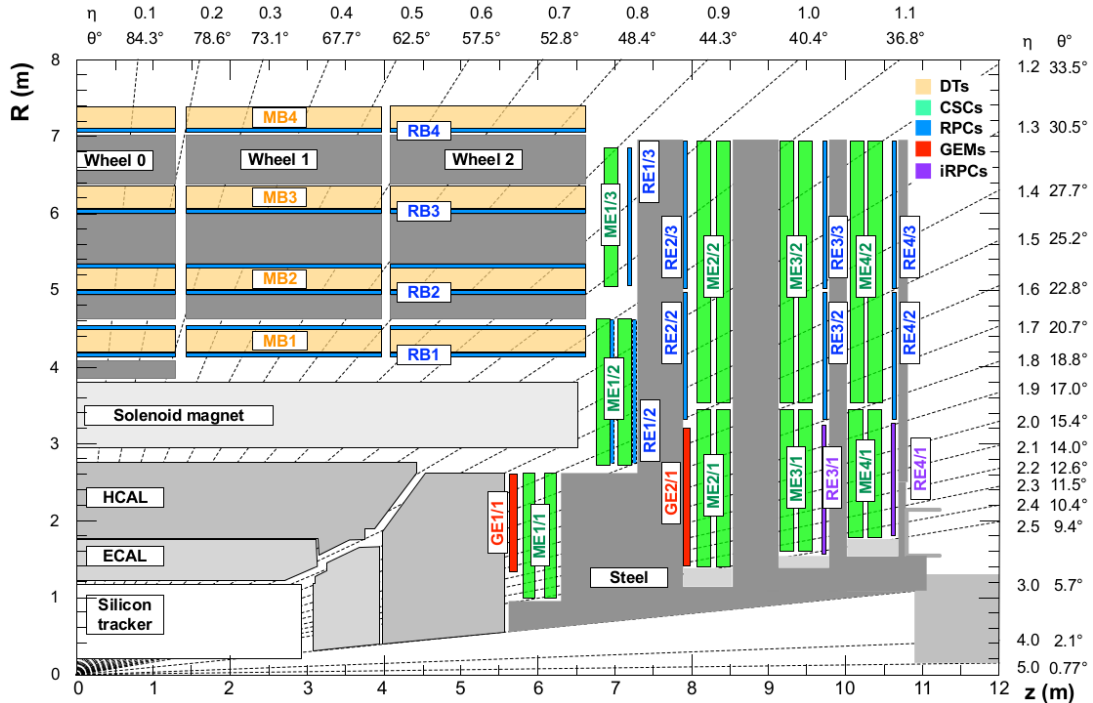


Figure 3.13: Section of CMS detector, in the plane ( $r, z$ ), parallel to the beamlime, that emphasizes the location of the muon detectors, in particular: Drift Tubes (DT, in yellow); Cathode Strip Chambers (CSC, in green); Resistive Plate Chambers (RPC, in blue).

### 227 3.2.6.2 The Cathode Strip Chambers

228 Cathode Strip Chambers cover a region of  $0.9 < |\eta| < 2.4$ , overlapping with the DT in the pseudorapidity  
 229 range  $0.9 < |\eta| < 1.2$ . The anodic wires inside each CSC are installed in six planes, with the aim  
 230 of measuring the radial coordinate; the wire planes are perpendicularly crossed by cathodic strips,  
 231 disposed along the radial direction to measure the  $\phi$  coordinate. Ionization electrons produced  
 232 by muons passing through the gas mixture in the chambers migrate from the anodes, inducing a  
 233 charge distribution on the cathodes, from which the azimuthal coordinate can be reconstructed.  
 234 The spatial resolution in the  $r$  coordinate is  $200 \mu\text{m}$ , and it is  $75 - 150 \mu\text{m}$  in the  $(r, \phi)$  plane. CSCs  
 235 are arranged in four disks and in three concentric rings.

### 236 3.2.6.3 The Resistive Plate Chambers

237 Resistive Plate Chambers are located both in the barrel (disposed in six layers) and in the endcap  
 238 region (three layers), up to a pseudorapidity of  $|\eta| < 1.6$ . These gas detectors are charged at very  
 239 high voltages, in order to work in the avalanche ionization mode. The plastic resistive plates are  
 240 equipped with readout strips. The spatial resolution of the detector is low (1-2 cm), but the fast  
 241 timing response (2-3 ns) and good time resolution (1 ns) allow to employ RPCs as an additional  
 242 triggering system and to profit of a precise measurement of the bunch-crossing time.

### 243 3.2.7 The trigger system and data acquisition

244 The CMS trigger system [8] has been designed considering the high instantaneous luminosity, such  
 245 that it can provide a fast response and it allows to reduce the nominal event rate of 40 MHz in pro-

## 3.2 CMS detector

---

ton proton collision. The complexity of the CMS detector and the very high number of readout channels result into a huge amount of data per event, approaching the order of few MB per bunch crossing, hence 40 TB per second. The processes of handling and recording data are currently limited by the employed technology to a frequency of  $\sim$ 100 Hz. Applying online selections to skim the events that are going to be written on tape, without rejecting interesting signals of hard processes and rare phenomena, is therefore a crucial and challenging point for every data analysis. Events are filtered by trigger selections at different levels: the Level-1 (L1) trigger is an hardware device, that allows to reduce the event rate from 40 MHz to the order of 100 kHz; the High Level Trigger (HLT) is a set of software algorithms that skims the event rate down to few hundred Hz. Once the trigger decisions are taken, the final events are handled by the Data Acquisition System (DAQ), that collects the informations coming from the sub-detectors and sends them to the storage unities.

257 **3.2.7.1 The Level-1 trigger**

258 The L1 trigger is an hardware device composed by customized electronics, and it accesses the information coming from the calorimeters and the muon system, while the tracker is not considered  
259 given the excessively large bandwidth needed by its readout channels. The L1 trigger performs a  
260 first raw local reconstruction of each object, called “trigger primitive”. The L1 trigger is composed  
261 by three subsystems: the calorimeter trigger, the muon trigger (divided in three independent sub-  
262 subsystems for each muon sub-detector, DTs, RPCs and CSCs), and the global trigger, that combines  
263 the informations of the former subsystems. The best quality trigger primitives reconstructed by the  
264 calorimeter and muon detectors (namely, roughly reconstructed electrons, photons, muons, jets,  
265 jets coming from the hadronic decays of tau leptons, and missing transverse energy) are handled  
266 by the global trigger, which takes the decision of discarding or keeping the event every  $3.2\ \mu s$ . The  
267 simplest trigger selections require the presence of a single object, whose energy or transverse mo-  
268 mentum is higher than a certain threshold; more complicated triggers involve multiple objects or  
269 geometrical selections, that can be performed in parallel up to 128 simultaneous requirements.  
270

271 **3.2.7.2 The High Level Trigger**

272 The HLT skims the L1 output rate down to few hundreds of Hz by applying a set of algorithms im-  
273 plemented in the same software used for the offline analysis, consisting in an event reconstruction  
274 performed exploiting the whole informations coming from all sub-detectors. The computing time  
275 is still a crucial factor, hence selections applied to HLT physics objects are generally less accurate  
276 than those of the offline analysis; furthermore, HLT can discard the event even before its full recon-  
277 struction (*i.e.* by looking only at certain region of the detectors). Events filtered by the HLT decisions  
278 are assigned to precise trigger paths and recorded in different categories of datasets.

279 **3.2.7.3 Data acquisition, computing and storage**

280 The DAQ system deals with the storage, transfer and handling of the data collected by CMS; it also  
281 supports and stores the data simulations and calibrations of the sub-detectors. The CMS compu-  
282 tational resources are located in worldwide distributed data nodes, called Tiers. The CMS software  
283 (CMSSW) is based on an object oriented architecture (mainly C++). The basic unity of every data,  
284 both real and simulated ones, is the Event, that could contain very rough informations (RAW data  
285 format) or higher level refined objects (AOD, Analysis Object Data) where all the calibrations and  
286 corrections needed to properly deal with the final physics objects are already in place. Data are  
287 handled by C++ or python modules, and the outputs are written in ROOT [9] files.

**288 3.2.8 Particle Flow event reconstruction**

289 The particle flow (PF) algorithm [10] aims at identifying and reconstructing each particle produced  
 290 by the proton-proton collisions, combining the informations coming from all the CMS sub-detectors.  
 291 It is particularly suitable to improve the reconstruction of jets, missing transverse momentum (used  
 292 to identify neutrinos) and hadronically decaying tau leptons.  
 293 The association of the informations is performed at different stages. The reconstruction of the  
 294 charged particles in the silicon detector is performed with an iterative algorithm, and the recon-  
 295 structed object is called a tracker track. Then, a clustering algorithm is performed to collect and  
 296 combine the energy deposits in the calorimeters, in such a way to distinguish neutral from charged  
 297 particles, reconstruct their directions, and improve the energy measurement of the very energetic  
 298 charged particles, whose tracks are less bended by the magnet and hence less precisely determined.  
 299 The last informations are provided by the hits collected in the muon system. The three sets of re-  
 300 constructions are then combined with a link algorithm, that aims at associating tracker tracks to  
 301 calorimeter clusters and muon hits with geometrical criteria. A track in the silicon detector is linked  
 302 to a calorimeter cluster if the extrapolated position lies in the cluster itself. Similarly, clusters in dif-  
 303 ferent calorimeters are linked when the position in the more granular calorimeter (*i.e.* ECAL) lies in  
 304 the envelope of the clusters in the less granular calorimeter (*i.e.* HCAL). The decision of linking a  
 305 tracker track to a muon track is based on the  $\chi^2$  of a global fit between the two tracks.  
 306 The particle flow algorithm then interprets the collected and linked informations as different par-  
 307 ticles. Muons are identified by the combination of a track in the silicon detectors and a track in the  
 308 muon chambers. Photons are determined directly by ECAL clusters. Electrons energies and posi-  
 309 tions are measured by ECAL clusters, linked to a corresponding tracker track, and considering all the  
 310 energy clusters produced by the bremsstrahlung photons radiated while interacting with the detec-  
 311 tor material. The hadrons are identified by the tracks (if charged) linked to the corresponding ECAL  
 312 and HCAL clusters. The hadron energy resolution, 10% at 100 GeV combining ECAL and HCAL, is  
 313 such that neutral hadrons can be distinguished as an energy calorimetric excess when overlapped  
 314 by a charged hadron occupying the same calorimetric towers. Finally, the missing transverse mo-  
 315 mentum is defined as the negative sum of the transverse momenta of all the particles identified by  
 316 the PF algorithm.

317

**318 3.2.9 Physics objects**

**319 3.2.9.1 Track reconstruction**

320 The reconstruction of the trajectories of the charged particles passing through the CMS detector is  
 321 performed by multiple iterations of the Combined Track Finder algorithm, that is based on a Kalman  
 322 filter approach [11]; given the high multiplicity of particles produced at each bunch crossing and the  
 323 multiple scatterings in the detector materials, tracking represents a challenging task. The CTF al-  
 324 gorithm builds a track starting from the so-called seeds, namely triplets of hits collected in the pixel  
 325 detector inner layers, or couples of hits if the track originates from the interaction point. The ini-  
 326 tial guess of the track given by the seeds is then extrapolated to the outer layers: if other hits are  
 327 found to be compatible with the trajectory hypothesis ( $\chi^2$ -based hypothesis test), they are added to  
 328 the track. Once the outer layers are reached, another reconstruction is performed backward, in or-  
 329 der to clean the track from spurious hits and enhance the tracking efficiency. The final collected hits  
 330 are re-fitted with Kalman filter and more precise algorithms, in order to improve the quality of the  
 331 measurement. If two tracks share more than a half of their hits, the worst quality track is rejected.  
 332 The track reconstruction efficiency for particles with  $p_T > 0.9$  GeV is 94% in the barrel and 85% in

333 the endcap region [4].

334

335 **3.2.9.2 Vertices reconstruction**

336 The reconstruction of the vertices at each bunch crossing is performed in steps. Primary vertices  
 337 are originating from the proton proton collisions, whilst secondary vertices are due to long-lived  
 338 particles (heavy quarks and  $\tau$  leptons). The starting point of the procedure is clustering the re-  
 339 constructed tracks originating from the primary vertex; the decision is taken by the deterministic  
 340 annealing algorithm [12], taking as input the longitudinal impact parameter. The algorithm allows  
 341 to distinguish vertices separated down to 1 mm. The second step is run by the adaptive vertex fit-  
 342 ter [13], that measures the position of the vertex for the chosen set of tracks. The algorithm is based  
 343 on an iterative re-weighted Kalman filter, that down-weights the wrongly associated tracks not com-  
 344 patible with the considered vertex. The primary vertex is selected as the vertex where the sum of the  
 345  $p_T^2$  of the associated tracks is the largest. The spatial resolution on the vertex position is 10-40  $\mu\text{m}$   
 346 in the  $(r, \phi)$  plane, and 15-50  $\mu\text{m}$  in the longitudinal coordinate.

347 **3.2.9.3 Electrons and photons reconstruction**

348 Electrons are reconstructed [14] combining a track with the energy deposits clustered in the ECAL,  
 349 due to the showering of the electron through the detector and the emission of bremsstrahlung pho-  
 350 tons. The combination can proceed both from the silicon detector in the outgoing direction and in  
 351 the opposite way: the tracker seeding as starting point is suitable for low energy electrons, whose  
 352 trajectories are less bended and hence more accurately measured by the tracker system; the group-  
 353 ing of ECAL clusters (called superclusters) followed by a consecutive track extrapolation, performed  
 354 by taking into account the electron interaction with the detector material, is more efficient in case of  
 355 high energetic electrons, due to the higher resolution of the ECAL scintillating crystals. A Gaussian-  
 356 sum filter algorithm (GSF) [15] allows to properly take into account the effects of the bremsstrahlung  
 357 radiation, that is distributed not as a single Gaussian (standard Kalman filters) but rather as a sum  
 358 of Gaussian functions.

359 The identification of an electron relies on three groups of variables: observables built by combining  
 360 measurements performed in the silicon detectors and in the calorimeter; purely calorimetric ob-  
 361 servables; purely tracking informations. Different selections are used for electron candidates found  
 362 in the barrel or in the endcaps, and they can vary from loose criteria (high detection efficiency but  
 363 less purity, namely more contamination from object mis-identified as electrons) to tight criteria.  
 364 Data and Monte Carlo simulations reproducing  $Z$ ,  $\Upsilon$  and  $J/\Psi$  decays in  $e^+e^-$  are used to study the  
 365 optimal working points, each one targetting at a different purity.

366 The electron energy is determined correcting the raw energy measurement of the ECAL superclus-  
 367 ters by taking into account the effects of the losses due to radiation or gaps between the calorimeter  
 368 modules, and the pile-up contribution. The electron momentum resolution has been measured  
 369 in  $Z \rightarrow e^+e^-$  decays in Run 1 LHC data, and it varies from 1.7% to 4.5% depending on the pseu-  
 370 dorapidity range [16]. The electron isolation variable is defined as the  $p_T$  sum of the charged and  
 371 neutral particles lying in a cone of  $\Delta R = 0.3$  around the electron trajectory, divided by the transverse  
 372 momentum of the electron itself:

$$I_{\Delta R=0.3}^e = \frac{\sum_{\text{char. hadrons}} p_T + \max[0, \sum_{\text{neut. hadrons}} p_T + \sum_{\text{photons}} p_T - 0.5 \sum_{\text{pile-up char. hadrons}} p_T]}{p_T^e}; \quad (3.9)$$

373 the contribution of the pile-up charged particles is removed. The isolation variable is used to dis-  
 374 tinguish electrons coming from the leptonic decays of electroweak bosons (low  $I_{\Delta R=0.3}^e$ ) from elec-  
 375 trons coming from the decays of heavy fermions, when they are more likely produced in association  
 376 with light flavour jets and hence topologically close to calorimetric deposits due to hadrons (high  
 377  $I_{\Delta R=0.3}^e$ ).

378 Photons are reconstructed with the ECAL clusters only. Given their importance in the discovery of  
 379 the Higgs boson, dedicated studies have been performed both in data and in Monte Carlo simula-  
 380 tions reproducing the  $H \rightarrow \gamma\gamma$  process. Particular care has been taken in the treatment of the photon  
 381 conversions into electron-positron pairs while interacting with the tracker detector. Dedicated se-  
 382 lections allow to define different photon identification working points. Similarly to the case of the  
 383 electrons, the photon isolation variable can be defined. The photon energy resolution varies from  
 384 1% to 3%, depending on the  $\eta$  range [17].

#### 385 3.2.9.4 Muon reconstruction

386 A muon candidate can be built exploiting the hits collected in the silicon tracker (track) and in the  
 387 muon system (standalone muon) [18]. Each muon sub-detector (DTs, RPCs and CSCs) performs a  
 388 local reconstruction of the particle candidate; the informations from the three muon chambers are  
 389 combined with a Kalman filter approach.

390 Three different strategies are adopted to define a muon candidate in the CMS detector. A stan-  
 391 dalone muon is reconstructed by using only the local reconstruction in the muon chambers. A  
 392 tracker muon is built starting from a track in the silicon detector, that is extrapolated up to the muon  
 393 chambers, taking into account the multiple scattering and the energy loss through the material.  
 394 The tracker muon is defined if at least one segment, *i.e.* a short track built with CSCs or DTs hits,  
 395 is matched to the starting track. This technique is the most efficient for the reconstruction of low  
 396 energetic muons. A global muon is built starting from a standalone muon, and then its trajectory is  
 397 extrapolated towards the inner layer of the silicon detector and eventually matched to a track; this  
 398 approach is suitable for high energetic muons ( $p_T > 200$  GeV).

399 Different algorithms are used to assign a momentum to the muon candidate, in order to mitigate  
 400 the effects of bremsstrahlung, that becomes significant when the muon approaches energies of the  
 401 order of 1 TeV. The radiated photons generate spurious hits in the chambers and larger occupancy,  
 402 significantly deteriorating the momentum measurement.

403 Starting from 2016 LHC Run, the muon reconstruction takes into account the Alignment Position  
 404 Errors, namely the uncertainties due to the position of the muon chambers with respect to the sil-  
 405 icon detectors. The final resolution on the muon momentum measurement depends on the  $p_T$   
 406 and  $\eta$  of the candidate, and ranges from 1% for very low momenta, up to  $\sim 7\%$  ( $|\eta| < 0.9$ ) – 10%  
 407 ( $1.2 < |\eta| < 2.4$ ) [19].

408 The muon isolation  $I_{\Delta R=0.4}^\mu$  is defined similarly to the electron isolation, but by taking into account  
 409 a larger cone  $\Delta R = 0.4$  around the muon direction.

#### 410 3.2.9.5 Jet reconstruction

411 The nature of the strong interaction is such that coloured partons, namely quarks and gluons, are  
 412 forced to aggregate to form a color-neutral hadron, in the process called hadronization. Therefore,  
 413 partons cannot be observed as free particles in a detector, but rather as collimated jets of hadronic  
 414 particles.

415 Jets are reconstructed starting by the PF candidates in the event. The charged hadron subtraction al-  
 416 gorithm (CHS) removes candidates not associated to the primary vertex in order to suppress pile-up

### 3.2 CMS detector

---

417 contributions [20]. The remaining particles are used as input to jet clustering algorithms to recon-  
 418 struct particle-flow jets. The jets are clustered using the FASTJET package [21] with the anti- $k_T$  jet  
 419 sequential clustering algorithm [22]. A sequential clustering algorithm is designed to be infrared  
 420 and collinear safe, namely, if the final state particles undergo a soft emission or a collinear gluon  
 421 splitting, the number and shapes of the jets should not change. The starting point of a sequen-  
 422 tial clustering algorithm is the definition of the distances between two particles  $i$  and  $j$ , and the  
 423 distance of a given particle  $i$  from the beam-spot  $B$ :

$$d_{ij} = \min(p_{T,i}^{2a} p_{T,j}^{2a}) \frac{R_{ij}^2}{\Delta R^2}, \quad (3.10)$$

$$d_{iB} = p_{T,i}^{2a}$$

424 where  $p_{T(i,j)}$  are the transverse momenta of the particles,  $R_{ij}^2 = (\mathcal{Y}_i - \mathcal{Y}_j)^2 + (\phi_i - \phi_j)^2$  is the angular  
 425 distance between the particles,  $a$  is an exponent depending on the clustering algorithm chosen,  
 426 and  $\Delta R$  is the clustering parameter. The algorithm then operates as follows:

- 427 • it computes all the possible combinations of distances  $d_{ij}$  and  $d_{iB}$  and it finds the minimum;
- 428 • if the minimum is  $d_{ij}$ , the four-momenta of the particles  $i$  and  $j$  are summed up in one can-  
 429 didate  $i j$ ;  $i$  and  $j$  are removed from the list of available particles, the distances are updated,  
 430 and the algorithm proceeds to re-calculate all the possible remaining  $d_{ij}$ ;
- 431 • the clustering stops when the smallest quantity is  $d_{iB}$ :  $i$  particle is defined as one jet, and it is  
 432 removed from the list of particles;
- 433 • this process is repeated until all the particles are assigned to a jet, that must be separated from  
 434 another jet at least by a distance  $R_{ij} > \Delta R$ .

435 If the anti- $k_T$  algorithm is applied, the exponent  $a = -1$ . This means that it tends to cluster high  $p_T$   
 436 particles first, given that the hard term dominates  $d_{ij}$  in equation 3.10. Since the soft particles have  
 437 lower impacts, the shape of the jet is not sensitive to the soft radiation and rather stable against the  
 438 softer pile-up contributions.

439 In this analysis, clustering parameters of  $\Delta R = 0.8$  and  $\Delta R = 0.4$  will be used to define the “fat”-jets  
 440 or AK8 jets, and the “standard”-jets or AK4 jets. In order to avoid double-counting of PF candidates,  
 441 AK4 jets are considered only if the angular separation from the leading AK8 jet is larger than  $\Delta R >$   
 442 0.8.

443 Since the detector response to different particles is non-linear, particular care should be taken in  
 444 the assignment of the measured momentum of the clustered jet to the corresponding true value  
 445 of the original parton [23]. A set of jet energy corrections (JECs) are applied sequentially and with  
 446 a fixed order. Each correction consists in a rescaling of the jet four-momentum, and it takes into  
 447 account different effects that are factorized.

- 448 • The L1 JECs remove the effect of the pile-up; they consist into an offset correction of the jet  
 449  $p_T$ . They are determined from Monte Carlo (MC) simulations of di-jet events produced by  
 450 strong interaction with and without pile-up events on top, and parametrized as a function of  
 451 kinematical variables (jet area, pseudorapidity and  $p_T$ ) and of the average  $p_T$  density per unit  
 452 area,  $\rho$ . Residual differences between data and the detector simulation are evaluated in data  
 453 collected with a random trigger, called zero bias, applying the only requirement of the beam  
 454 crossing happening. Pile-up offset corrections are displayed in fig. 3.14 (top left), as a function  
 455 of the jet pseudorapidity.

- The simulated response of the detector is not uniform over jet  $p_T$  and  $\eta$ . This effect is mitigated by the L2L3 MC-truth corrections. They are calculated in MC simulations of di-jet events, by taking into account the discrepancy between the reconstructed  $p_T$  of the jet and the true  $p_T$  at particle generator level (*i.e.*, before simulating the interaction of the parton showers with the detector), as a function of jet  $p_T$  and  $\eta$ . L2L3 scale factors describing the simulated jet response are reported in fig. 3.14 (top right), as a function of the jet pseudorapidity.
  - The small data-MC discrepancies ( $\sim 1\%$ ) left after applying the previous set of JECs are corrected by the L2 and L3 residual corrections. The L2Residuals are calculated in di-jet events, as a function of  $p_T$ . The L3Residuals are calculated in  $Z \rightarrow (\mu\mu, ee) + \text{jet}$  events, photon + jet events and multijet events, as a function of  $\eta$  and  $p_T$  [23]. Data-MC scale factors for L2L3Residuals are displayed in fig. 3.14 (bottom), as a function of the jet  $\eta$  and  $p_T$ .
  - An optional correction, not used in this analysis, is the L5 flavour-dependent correction, that is extracted from MC simulations.
- Each jet energy correction is determined with an uncertainty, and reported in fig. 3.15 for 2015 data, as a function of  $p_T$  and  $\eta$  of the jet. The total uncertainty for jets with  $p_T$  larger than 30 GeV (100 GeV) is smaller than 3% (1%) in the barrel, and up to 5% (3%) in the endcaps [24].
- An additional effect that must be taken in account in the analysis is the discrepancy in the jet energy resolution (JER) observed in data and in Monte Carlo samples. A smearing procedure is applied in MC simulations (described in detail in sec. ??), in order to restore a better agreement. Jet energy resolutions in Monte Carlo simulations are displayed in fig. 3.16 (top), as a function of the jet  $p_T$  and the average number  $\mu$  of reconstructed primary vertices, considering central (left) and forward (right) jets. The resolution is stable against the pile-up for jet  $p_T > 100$  GeV, and it ranges from 10% at 100 GeV, down to 4% at 1 TeV [24]. In fig. 3.16 (bottom), data-MC smearing scale factors are reported as a function of  $\eta$ .

### 3.2.9.6 Tau reconstruction

Tau leptons have a very small lifetime ( $\sim 3 \times 10^{-13}$  s), hence they decay before reaching the pixel detector and they can only be reconstructed through their decay products. Approximatively 60% of the times,  $\tau$  leptons decay in hadrons, hence they are reconstructed as small collimated jets in the CMS detector. The main decay modes of the hadronic tau,  $\tau_h$ , are one or three charged mesons (mainly  $\pi^\pm$ ), also in association with a  $\pi^0$  decaying in a couple of photons, and a  $\tau$  neutrino. Hence, photons and charged hadrons are the main ingredients of dedicated algorithms to perform the  $\tau_h$  reconstruction and identification, in order to distinguish them from quark and gluon-initiated jets. The main CMS  $\tau_h$  reconstruction algorithm, Hadron Plus Strips (HPS) [25], is particle-flow based. HPS builds the tau candidate from a PF jet, clustered with the anti- $k_T$  algorithm with  $\Delta R = 0.5$ , and it reconstructs the  $\pi^0 \rightarrow \gamma\gamma$  decays within the jet cone, by taking into account the photon conversions in the silicon detector. The exploitation of the PF informations is such that the HPS algorithm shows stable performances in the reconstruction of the  $\tau_h$  energy as a function of the energy itself. The  $\tau_h$  candidate is required to be isolated, namely no energy deposits other than the  $\tau$  decay products should be present in the tau cone. Depending on the low threshold set to consider the surrounding particles as included in the cone, different isolation working points can be defined. With the looser working point, the probability of mis-identifying a quark or gluon jet as a tau is around 1% [25].

### 3.2.9.7 b-jets tagging

The bottom quark plays a fundamental role in numerous standard model processes, *i.e.* the physics related to the top quark (that decays into a W and a b-quark with a branching fraction of 100%) and

### 3.2 CMS detector

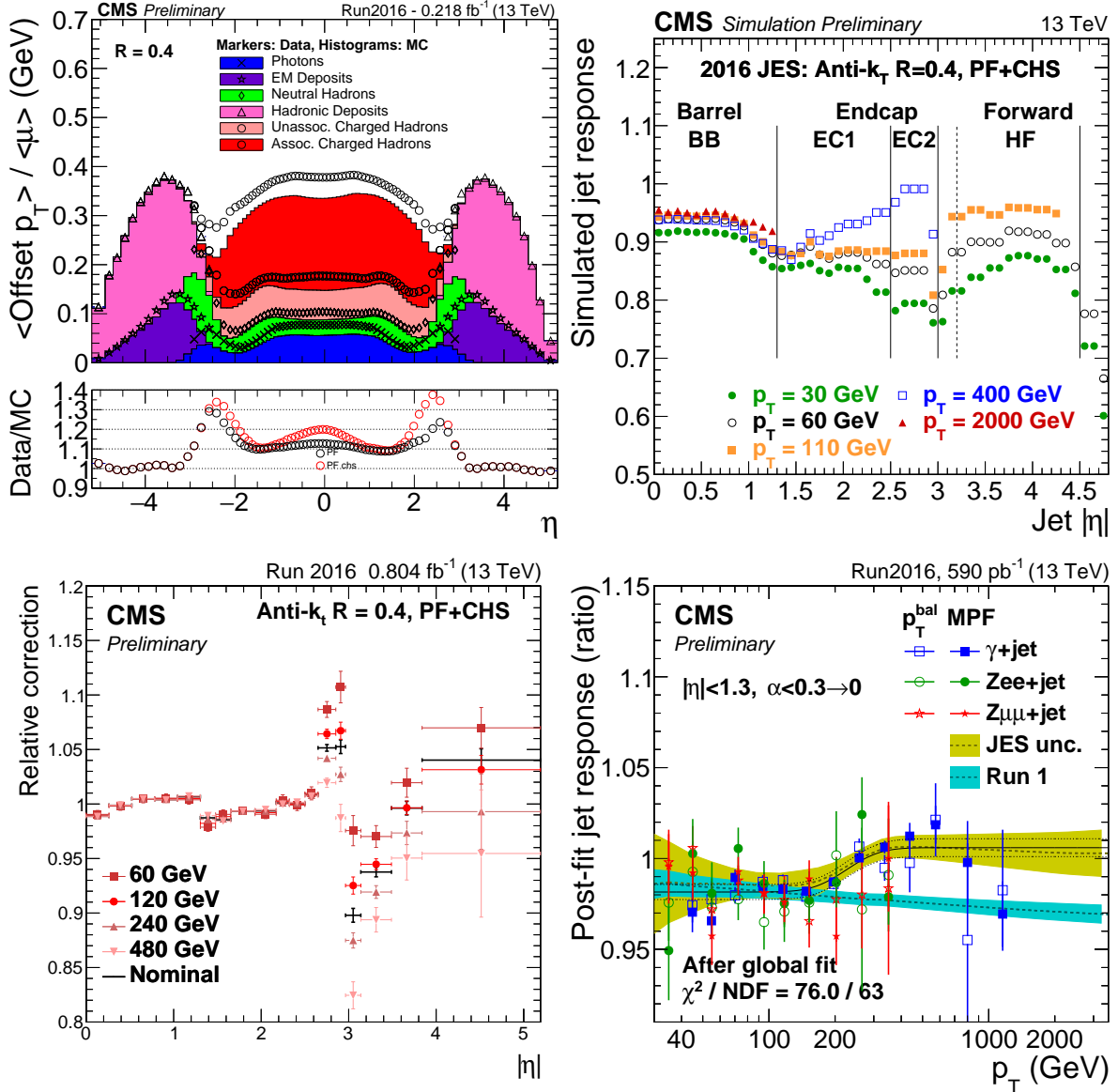


Figure 3.14: Top left: average  $p_T$  offset due to additional pile-up events, measured both in data and in MC simulations, as a function of the jet pseudorapidity. Top right: simulated jet response (L2L3 MC-truth corrections), as a function of the jet pseudorapidity. Bottom left: L2L3 residual data-MC corrections, evaluated on di-jet events, as a function of the jet  $\eta$ . Bottom right: L2L3 residual data-MC corrections, evaluated on di-jet and  $Z/\gamma$  + jet events, as a function of the jet  $p_T$ .

the Higgs boson (decaying into  $b\bar{b}$  with a branching fraction  $\sim 60\%$ ). Many algorithms have been exploited by the CMS collaboration, with the aim of distinguishing a b-quark initiated jet and jets originating from light quarks or gluons [26]. The most remarkable feature of the b-quark is the long lifetime ( $\sim 1.5$  ps), that has the experimental consequence of a displaced decay (few mm) with respect to the primary vertex. The direct leptonic decays of the b-quark (into  $\mu$  and  $e$ ) or the cascade leptonic decays involving c-quarks give an additional handle to its identification.

Given the high spatial resolution of the silicon detector, track reconstruction is a key point of the b-tagging procedure. Tracks inside a jet candidate must satisfy criteria related not only to their quality but also on their distance from the interaction point. The track impact parameter is the distance

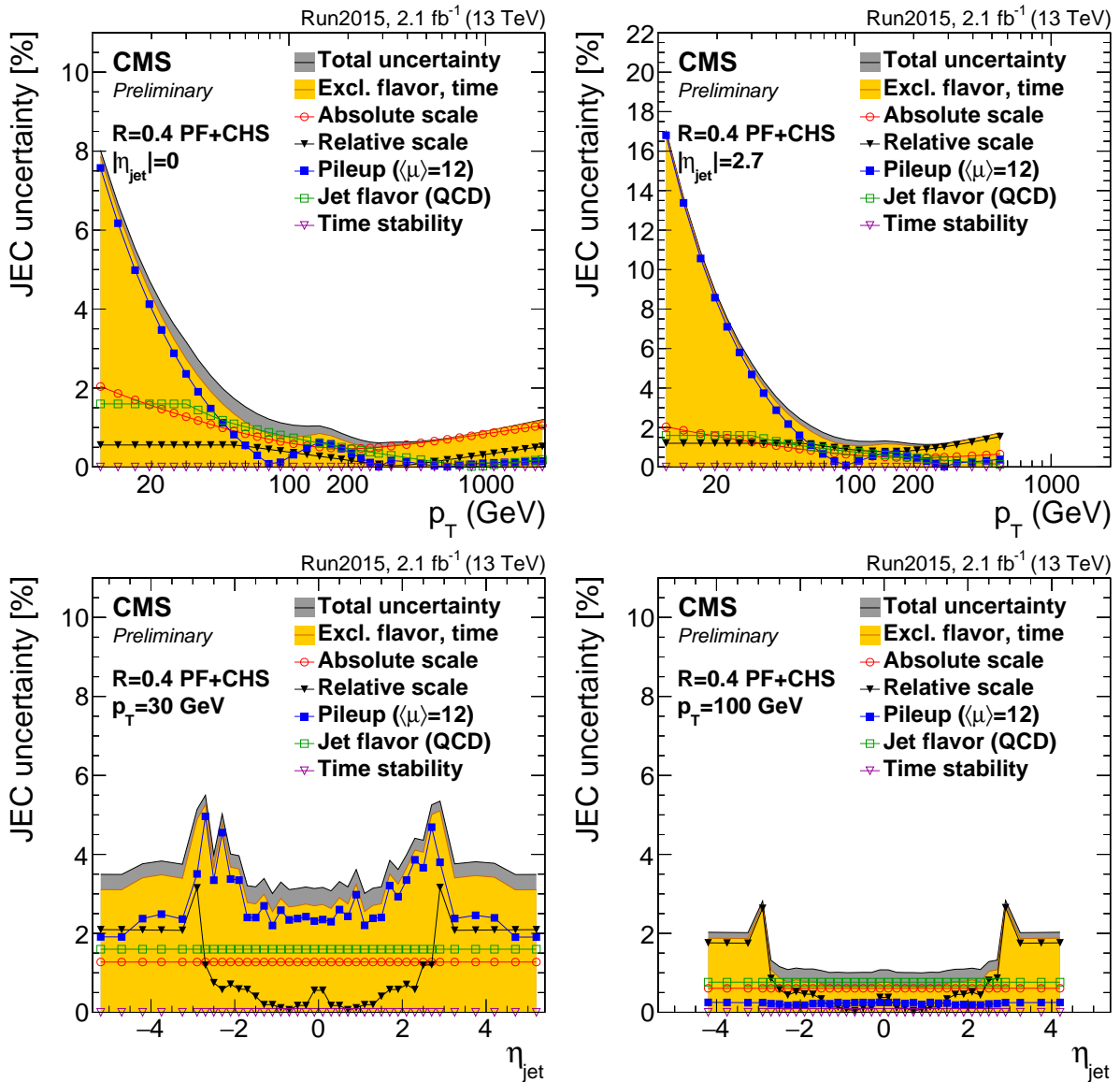


Figure 3.15: Jet energy corrections uncertainties, as a function of jet  $p_T$  (top) and  $\eta$  (bottom), calculated in 2015 data. The yellow histograms report the convolution of the uncertainties applied in the analysis.

509 between the primary vertex and the coordinate of closest approach. Tracks that are too far from  
 510 the interaction point are discarded, in order to suppress the pile-up contributions. The Combine  
 511 Secondary Vertex (CSV) algorithm [27] sorts jet candidates in categories, based on the number of  
 512 reconstructed secondary vertices (one reconstructed secondary vertex, no secondary vertices but  
 513 two tracks with high impact parameters, and the remaining cases). A multivariate approach allows  
 514 to train the algorithm over the categories, considering as discriminating variables both tracking in-  
 515 formations (numbers and properties of the tracks) and their relations with the secondary vertex re-  
 516 construction (impact parameters; angular, linear, 2D and 3D distances of the vertex from the tracks  
 517 and the jet axis; invariant mass of the charged particles associated to the secondary vertex).  
 518 By tuning the selections, working points with different efficiencies have been set. The loose work-  
 519 ing point, used in this analysis, has a 90% signal efficiency and a 40% mis-identification rate. The

### 3.2 CMS detector

---

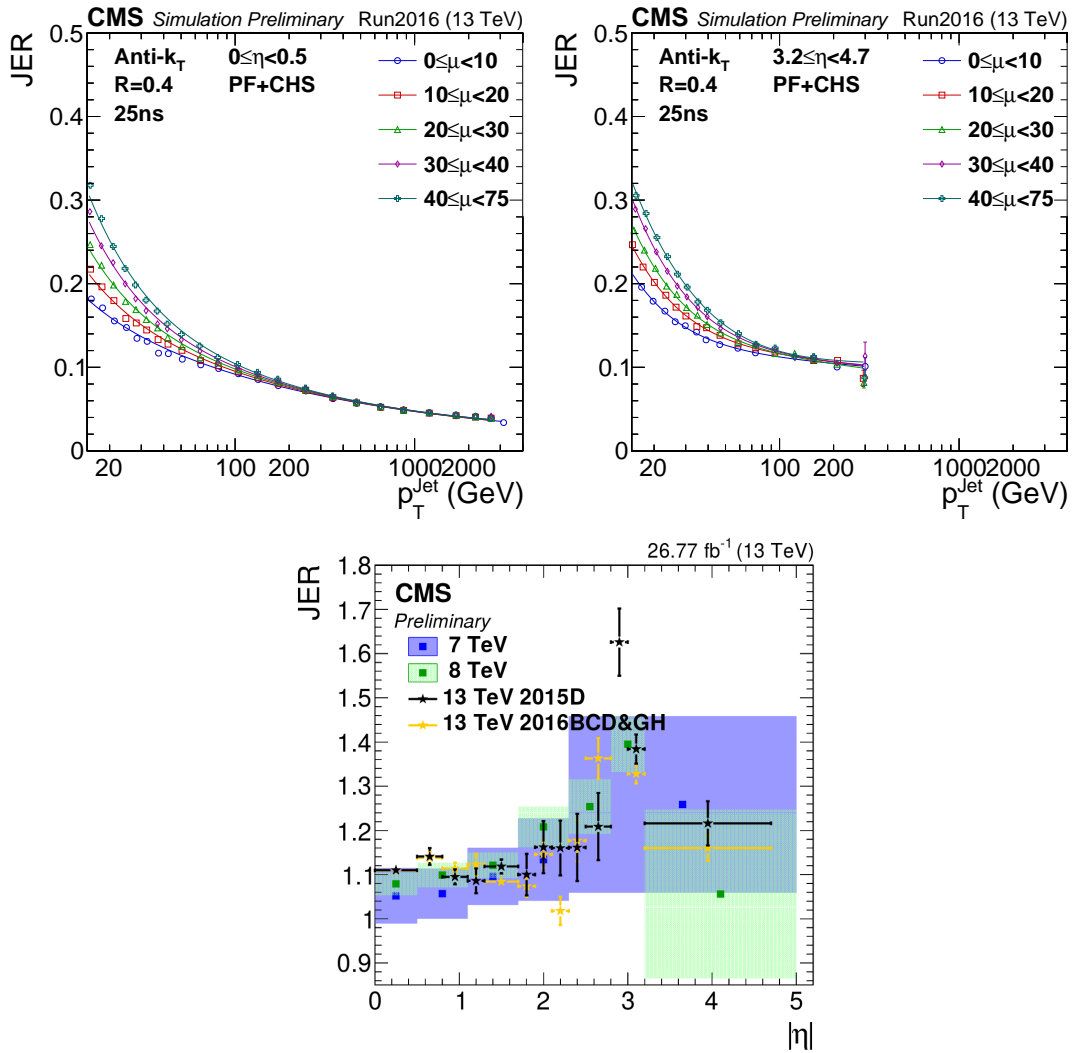


Figure 3.16: Top: jet energy resolution in MC simulations, as a function of the jet  $p_T$ . Different curves represent a different average number of primary vertices per event ( $\mu$ ). Bottom: data-MC scale factors, as a function of the jet  $\eta$ , measured in 2016 data (yellow dots).

520 b-tagging efficiency is different in data and in simulations. Multiplicative scale factors are calcu-  
521 lated in events enriched in b-quark jets.

522

523 **3.2.9.8 Missing transverse energy reconstruction**

524 Neutrinos can interact with the other particles only via the electroweak interactions; hence, when a  
525 neutrino is produced in the proton-proton collisions, it passes through the CMS experiment, unde-  
526 tected. Its only experimental signature is the momentum imbalance ( $\vec{p}_T^{\text{miss}}$ ) in the transverse plane  
527 ( $r, \phi$ ). The magnitude of  $\vec{p}_T^{\text{miss}}$  vector is also called missing transverse energy,  $E_T^{\text{miss}}$ . Given its def-  
528 initition, it is evident that  $E_T^{\text{miss}}$  is a delicate variable to deal with, since it depends on all the other  
529 objects, on their imperfect measurements, on the detector noise and the pile-up events.

530 The PF  $E_T^{\text{miss}}$  is the negative sum of the transverse momenta of the PF candidates reconstructed in  
531 the event. Inefficiencies in the tracker reconstruction and non-linear responses of the calorimeters

532 can be corrected by propagating the jet energy corrections to  $\vec{p}_T^{\text{miss}}$  [28]:

$$\vec{p}_T^{\text{miss,corr}} = \vec{p}_T^{\text{miss}} - \sum_{j \in \text{jets}} (\vec{p}_{T,j}^{\text{corr}} - \vec{p}_{T,j}^{\text{raw}}), \quad (3.11)$$

533 where "corr" ("raw") is related to corrected (raw)  $p_T$  of the considered jet. This correction is known  
 534 as the "Type-I" correction to  $E_T^{\text{miss}}$ . Jets included in the calculation are AK4 with CHS algorithm applied  
 535 to remove the pile-up contribution, they must have  $p_T > 15$  GeV and less than 90% of their  
 536 energy deposited in the electromagnetic calorimeter. If a muon lies in the jet cone, it is subtracted  
 537 from the jet and added after the  $p_T$  correction. A similar correction is performed to correct  $\vec{p}_T^{\text{miss}}$  at  
 538 trigger level; in this case, a jet  $p_T$  threshold of 35 GeV is chosen.

539 The  $E_T^{\text{miss}}$  uncertainty depends on the topology of the final state. It is calculated per-event by factorizing  
 540  $\vec{p}_T^{\text{miss}}$  in components: electrons, photons, muons, taus, jets, jets with  $p_T < 10$  GeV and all  
 541 the remaining PF candidates that are not clustered inside jets, called unclustered energy. The momen-  
 542 tum of every object is varied within its uncertainties (namely, the energy scale and resolution),  
 543 and the effects are propagated to  $\vec{p}_T^{\text{miss}}$ . The most significant contributions in the unclustered en-  
 544 ergy is due to neutral PF hadrons and hadrons reconstructed in the forward hadronic calorimeter.  
 545 The effects related to jet energy scale and unclustered energy scale are measured on simulation, in  
 546 events with a top and an anti-top quarks, and amounts to 5% and 30% respectively [28].

547

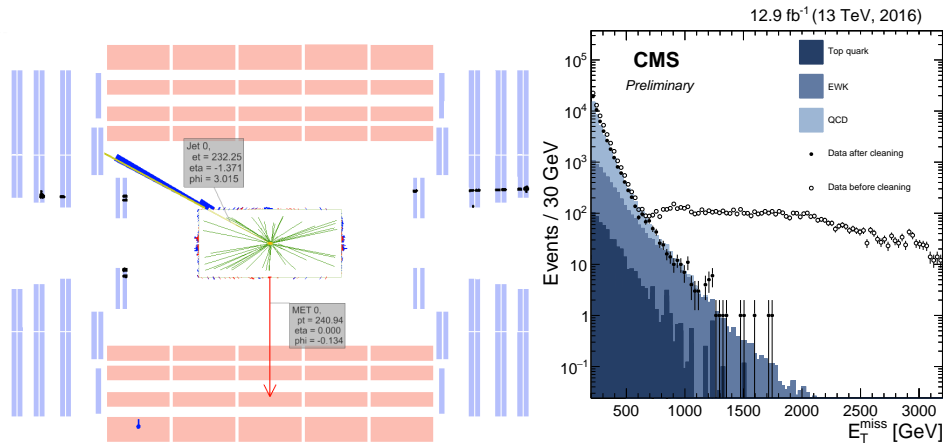


Figure 3.17: Left: event display of beam halo particles hitting the CSC detector. Right: comparison of data and simulations (histograms) when di-jet events are selected, before (open markers) and after (filled markers) anomalous  $E_T^{\text{miss}}$  cleaning algorithms have been applied on data.

548 Many instrumental effects can give rise to anomalous  $E_T^{\text{miss}}$  determination: they have been studied  
 549 in detail during Run1 [29,30] and Run2 [28], and they are mainly caused by ECAL and HCAL. In ECAL,  
 550 anomalous  $\vec{p}_T^{\text{miss}}$  is caused by particles hitting the sensors of the photodetectors, or by beam halo  
 551 particles (namely, particles produced in spurious proton interactions before reaching the interac-  
 552 tion point in the detector) showering inside the calorimeter, or by losses due to ECAL dead cells. An  
 553 event display representing beam halo muons hitting the CSC detector is showed in fig. 3.17 (top).  
 554 In HCAL, spurious  $\vec{p}_T^{\text{miss}}$  can be related to noise in the hybrid photodiodes and readout frontend. In  
 555 HF, missing  $p_T$  can be related to particles lost in the light guides and photomultipliers. Additional  
 556 anomalous  $E_T^{\text{miss}}$  can be produced by low quality muon tracks, that are not linked to segments re-  
 557 constructed in the muon chambers by the PF algorithm. These tracks are then classified as charged  
 558 hadrons, taken into account in the  $\vec{p}_T^{\text{miss}}$  calculation, and result into a large amount of fake  $E_T^{\text{miss}}$ .

### 3.2 CMS detector

---

559 Dedicated algorithms have been designed to identify and reject events with anomalous  $E_T^{\text{miss}}$ , and  
 560 they are consistently applied on data and simulations. In fig. 3.17 (right), Monte Carlo simulations  
 561 (coloured histograms) are compared to data before the algorithms removing the anomalous  $E_T^{\text{miss}}$   
 562 have been applied (open markers) and after the cleaning (filled markers): the spurious high- $\vec{p}_T^{\text{miss}}$   
 563 tail has been suppressed.

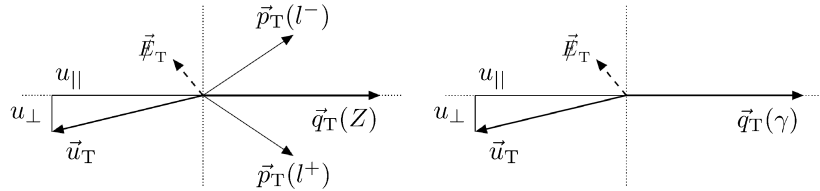


Figure 3.18: Left (Right): kinematics of  $Z \rightarrow \ell\ell$  (photon) events in the  $(r, \phi)$  plane;  $\vec{u}_T$  is the hadronic recoil,  $\vec{q}_T$  is the transverse momentum of the considered boson.

564 Performance of  $E_T^{\text{miss}}$  reconstruction are studied in events with a leptonic decay of a  $Z$  boson (in two  
 565 muons or in two electrons) or an isolated photon. The distributions of  $E_T^{\text{miss}}$  are showed in fig. 3.19,  
 566 separately for the three event categories. The hadronic recoil  $\vec{u}_T$  is defined in the transverse plane  
 567 as the vectorial sum of all the particle transverse momenta, except the momentum  $\vec{q}_T$  of the vector  
 568 boson considered ( $Z$  or  $\gamma$ ). From the momentum conservation, the following relation holds:

$$\vec{q}_T + \vec{p}_T^{\text{miss}} + \vec{u}_T = 0. \quad (3.12)$$

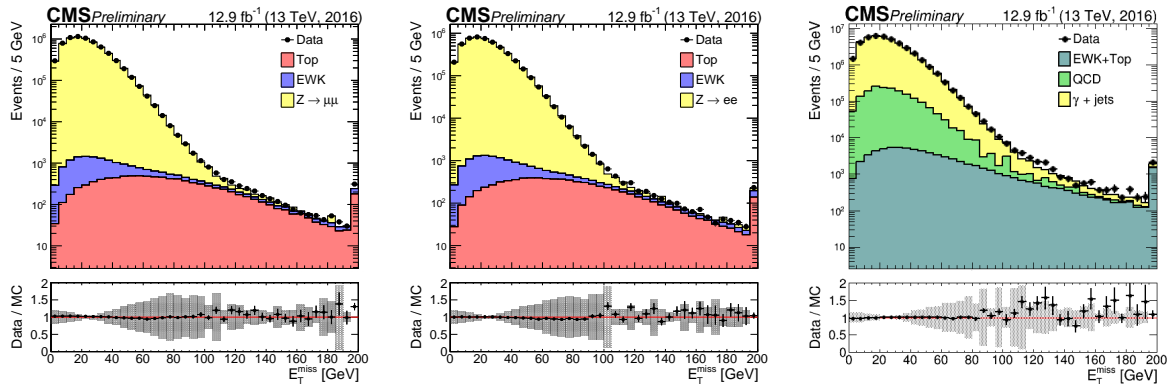


Figure 3.19: Data (black markers) and Monte Carlo (histograms) distributions of  $E_T^{\text{miss}}$  variable, in events reconstructing respectively a  $Z \rightarrow \mu\mu$  decay (left), a  $Z \rightarrow ee$  decay (center), an isolated photon (right).

569 The hadronic recoil is projected in the parallel and perpendicular directions with regards to  $\vec{q}_T$ . The  
 570 components  $u_{||}$  and  $u_{\perp}$ , along with the vectors described in eq.3.12, are schematically represented  
 571 in fig. 3.18. The  $E_T^{\text{miss}}$  response, defined as  $-\langle u_{||} \rangle / \langle q_T \rangle$ , is calculated as a function of  $q_T$  in data and  
 572 simulations (fig. 3.20, left). The distributions of the two components of the hadronic recoil,  $u_{||} + q_T$   
 573 and  $u_{\perp}$ , are modelled as Voigtian functions (the convolution of a Gaussian with a Breit-Wigner). The  
 574 resolution of each component is calculated as the full width at half maximum of the corresponding  
 575 Voigtian, and it is displayed in fig. 3.20 (center and right plots), as a function of  $q_T$ .

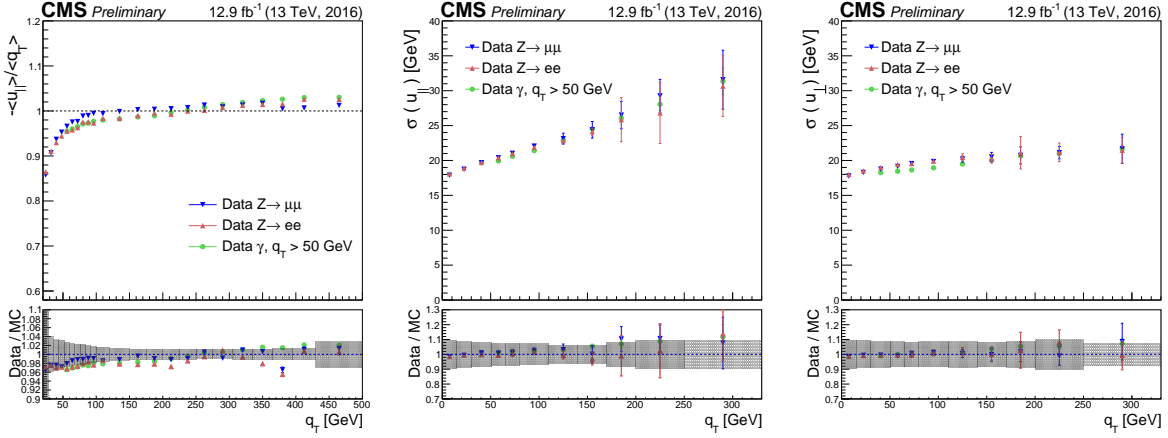


Figure 3.20: Left:  $E_T^{\text{miss}}$  response, as a function of the transverse momentum  $q_T$  of the vector boson considered in the event ( $Z$  decaying in  $\mu\mu$ ,  $Z$  in  $ee$  or a photon), measured on data. Center and right: resolution on the measurement of the parallel and perpendicular hadronic recoil in data, as a function of  $q_T$ .

### 576 3.3 ATLAS, ALICE, LHCb detectors

#### 577 3.3.1 ATLAS

578 ATLAS (A Toroidal LHC ApparatuS) [31] is a multi-purpose experiment, that shares the same scientific aims of CMS. The simultaneous observation of an Higgs boson-like particle at the two experimental facilities represented an irrefutable proof of the discovery of the Higgs boson.

581 ATLAS has a cylindrical shape (diameter of 25 m, length of 46 m) and weights 7000 tons. Like CMS,  
582 ATLAS is composed by many sub-detectors: trackers, calorimeters and muon system. The ATLAS  
583 magnetic field is provided by a solenoid, located inside the cylinder, and a big toroid, located outside  
584 the sub-detectors, able to reach a magnetic field of 2 T at the interaction point. The main differences  
585 among the two experiments are listed below.

- 586 • *Tracker* – the CMS tracker has a better  $p_T$  resolution (mainly due to the higher magnetic field):  
587  $\sigma_{p_T}/p_T \approx 5 \cdot 10^{-4} p_T + 0.01$  at ATLAS;  $\sigma_{p_T}/p_T \approx 1.5 \cdot 10^{-4} p_T + 0.005$  at CMS.
- 588 • *Electromagnetic calorimeter* – the CMS electromagnetic calorimeter is completely enclosed  
589 inside the solenoid, whilst ATLAS calorimeter is outside of the solenoid. The particles going  
590 through the solenoid suffer an energy loss and a consequent deterioration of the energy reso-  
591 lution. The CMS ECAL has an energy resolution of  $\sigma_E/E \approx 3\%/\sqrt{E}$ ; the ATLAS calorimeter  
592 has a sandwich structure (liquid argon and lead layers) and a resolution of  $\sigma_E/E \approx 10\%/\sqrt{E}$ .
- 593 • *Hadronic calorimeter* – the CMS HCAL is partly inside the solenoid, partly outside, depauper-  
594 ating the resolution. The ATLAS hadronic calorimeter (made of iron and plastic scintillator  
595 tiles) has an energy resolution  $\sigma_E/E \approx 50\%/\sqrt{E} + 0.03$  GeV; CMS HCAL has a resolution of  
596  $\sigma_E/E \approx 100\%/\sqrt{E} + 0.05$  GeV.
- 597 • *Muon system* – the peculiar geometry of the ATLAS muon system allows a better resolution of  
598 the standalone measurement of the muon momenta (*i.e.*, without using tracker and calorime-  
599 ters), that is around 10% at 1 TeV. CMS has better performance when combining the informa-  
600 tions coming from the inner detectors (7% at 1 TeV against the 35% for the standalone mea-  
601 surement).

602 **3.3.2 ALICE**

603 ALICE (A Large Ion Collider Experiment) [32] studies the heavy ion collisions (lead-lead) or proton-  
604 ion in order to explore the physics of the hadrons in high density (or temperature) regimes, when  
605 a new state of matter appears, the so-called quark-gluon plasma (QGP). The QGP played a crucial  
606 role in the very first instants of the life of the universe.

607 **3.3.3 LHCb**

608 LHCb (Large Hadron Collider beauty) [33] is a detector designed to study the b-quark properties, in  
609 particular the CP violation and other rare phenomena related to B hadrons. The final aim of these  
610 measurements is trying to solve the matter-antimatter asymmetry problem.

611 The three detectors are depicted in fig. 3.21.

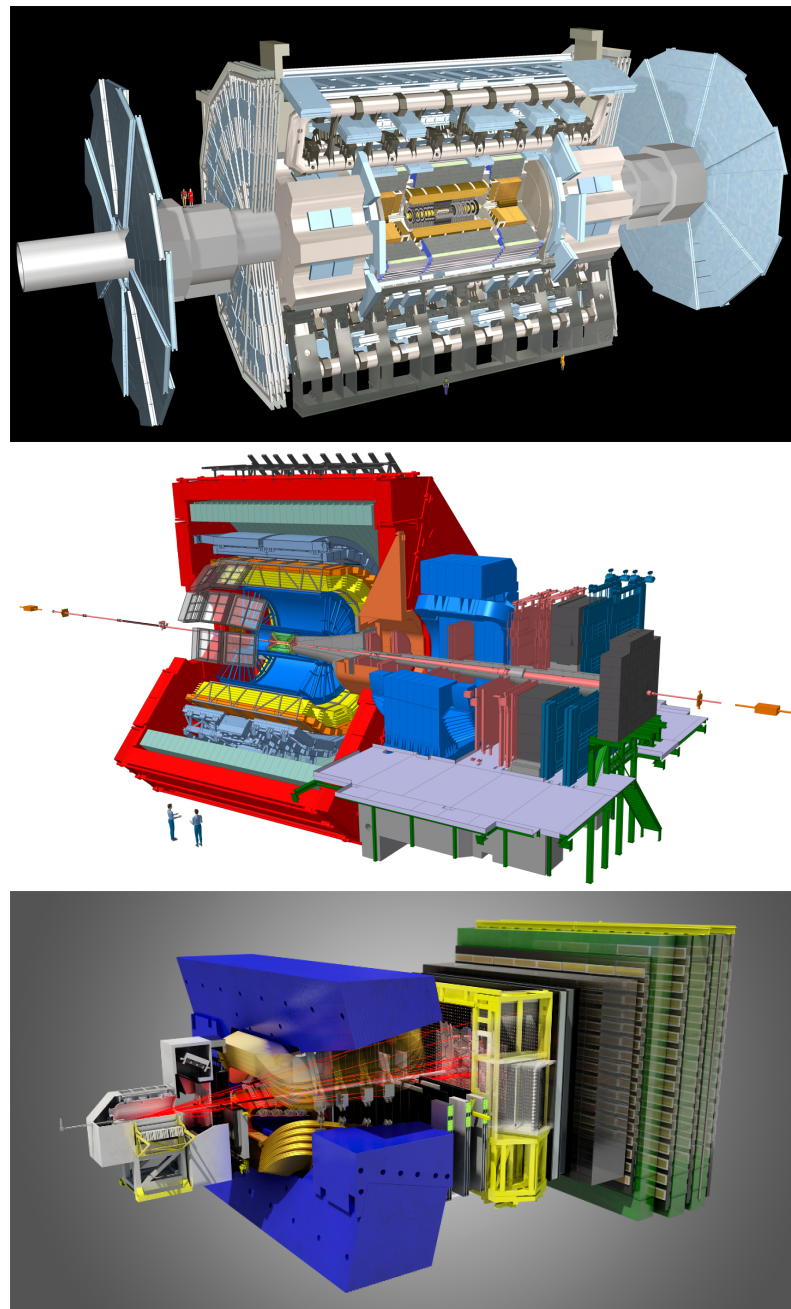


Figure 3.21: Top: the ATLAS experiment. Center: the ALICE experiment. Bottom: the LHCb experiment.

612

## Bibliography

613

614

- 615 [1] L. Evans and P. Bryant, “LHC Machine,” *JINST*, vol. 3, p. S08001, 2008.
- 616 [2] CMS Collaboration, “The CMS experiment at the CERN LHC,” *JINST*, vol. 3, p. S08004, 2008.
- 617 [3] CMS Collaboration, *The CMS tracker system project: Technical Design Report*. Technical Design Report CMS, Geneva: CERN, 1997.
- 618
- 619 [4] CMS Collaboration, “Description and performance of track and primary-vertex reconstruction with the CMS tracker,” *JINST*, vol. 9, no. 10, p. P10009, 2014.
- 620
- 621 [5] CMS Collaboration, *The CMS electromagnetic calorimeter project: Technical Design Report*. Technical Design Report CMS, Geneva: CERN, 1997.
- 622
- 623 [6] CMS Collaboration, *The CMS hadron calorimeter project: Technical Design Report*. Technical Design Report CMS, Geneva: CERN, 1997. The following files are from <a href=.
- 624
- 625 [7] CMS Collaboration, *The CMS muon project: Technical Design Report*. Technical Design Report CMS, Geneva: CERN, 1997.
- 626
- 627 [8] CMS Collaboration, *CMS The TriDAS Project: Technical Design Report, Volume 2: Data Acquisition and High-Level Trigger. CMS trigger and data-acquisition project*. Technical Design Report CMS, Geneva: CERN, 2002.
- 628
- 629
- 630 [9] R. Brun and F. Rademakers, “ROOT: An object oriented data analysis framework,” *Nucl. Instrum. Meth.*, vol. A389, pp. 81–86, 1997.
- 631
- 632 [10] CMS Collaboration, “Particle-flow reconstruction and global event description with the CMS detector.” Submitted to *JINST*, 2017.
- 633
- 634 [11] R. Fruhwirth, “Application of Kalman filtering to track and vertex fitting,” *Nucl. Instrum. Meth.*, vol. A262, pp. 444–450, 1987.
- 635
- 636 [12] K. Rose, “Deterministic annealing for clustering, compression, classification, regression, and related optimization problems,” vol. 86, pp. 2210 – 2239, 12 1998.
- 637
- 638 [13] R. Fruhwirth, W. Waltenberger, and P. Vanlaer, “Adaptive vertex fitting,” *J. Phys.*, vol. G34, p. N343, 2007.
- 639

- 640 [14] CMS Collaboration, “Energy Calibration and Resolution of the CMS Electromagnetic Calorimeter in  $p p$  Collisions at  $\sqrt{s} = 7$  TeV,” *JINST*, vol. 8, p. P09009, 2013. [JINST8,9009(2013)].
- 641
- 642 [15] W. Adam, R. Fröhlich, A. Strandlie, and T. Todor, “Reconstruction of Electrons with the Gaussian-Sum Filter in the CMS Tracker at the LHC,” 2005.
- 643
- 644 [16] CMS Collaboration, “Performance of Electron Reconstruction and Selection with the CMS Detector in Proton-Proton Collisions at  $s = 8$  TeV,” *JINST*, vol. 10, no. 06, p. P06005, 2015.
- 645
- 646 [17] CMS Collaboration, “Performance of Photon Reconstruction and Identification with the CMS Detector in Proton-Proton Collisions at  $\sqrt{s} = 8$  TeV,” *JINST*, vol. 10, no. 08, p. P08010, 2015.
- 647
- 648 [18] CMS Collaboration, “Performance of CMS muon reconstruction in  $p p$  collision events at  $\sqrt{s} = 7$  TeV,” *JINST*, vol. 7, p. P10002, 2012.
- 649
- 650 [19] CMS Collaboration, “Performance of muon reconstruction including Alignment Position Errors for 2016 Collision Data,” CMS Performance Note CMS-DP-2016-067, CERN, Geneva, Nov 2016.
- 651
- 652
- 653 [20] CMS Collaboration, “Pileup Removal Algorithms,” Tech. Rep. CMS-PAS-JME-14-001, CERN, Geneva, 2014.
- 654
- 655 [21] M. Cacciari, G. P. Salam, and G. Soyez, “FastJet user manual,” *Eur. Phys. J. C*, vol. 72, p. 1896, 2012.
- 656
- 657 [22] M. Cacciari, G. P. Salam, and G. Soyez, “The anti- $k_t$  jet clustering algorithm,” *JHEP*, vol. 04, p. 063, 2008.
- 658
- 659 [23] CMS Collaboration, “Determination of jet energy calibration and transverse momentum resolution in cms,” *Journal of Instrumentation*, vol. 6, no. 11, p. P11002, 2011.
- 660
- 661 [24] CMS Collaboration, “Jet energy scale and resolution performances with 13TeV data,” CMS Performance Note CMS-DP-2016-020, CERN, Geneva, Jun 2016.
- 662
- 663 [25] CMS Collaboration, “Performance of tau-lepton reconstruction and identification in CMS,” *JINST*, vol. 7, p. P01001, 2012.
- 664
- 665 [26] CMS Collaboration, “Identification of b quark jets at the CMS Experiment in the LHC Run 2,” CMS Physics Analysis Summary CMS-PAS-BTV-15-001, CERN, Geneva, 2016.
- 666
- 667 [27] CMS Collaboration, “Identification of b-quark jets with the CMS experiment,” *JINST*, vol. 8, p. P04013, 2013.
- 668
- 669 [28] CMS Collaboration, “Performance of missing energy reconstruction in 13 TeV pp collision data using the CMS detector,” 2016.
- 670
- 671 [29] CMS Collaboration, “Missing transverse energy performance of the CMS detector,” *JINST*, vol. 6, p. P09001, 2011.
- 672
- 673 [30] CMS Collaboration, “Performance of Missing Transverse Momentum Reconstruction Algorithms in Proton-Proton Collisions at  $p s = 8$  TeV with the CMS Detector,” 2012.
- 674
- 675 [31] ATLAS Collaboration, “The ATLAS Experiment at the CERN Large Hadron Collider,” *JINST*, vol. 3, p. S08003, 2008.
- 676

## BIBLIOGRAPHY

---

---

<sup>677</sup> [32] ALICE Collaboration, “The ALICE experiment at the CERN LHC,” *JINST*, vol. 3, p. S08002, 2008.

<sup>678</sup> [33] LHCb Collaboration, “The LHCb Detector at the LHC,” *JINST*, vol. 3, p. S08005, 2008.